Study of Dynamics of Mid-Infrared Quantum Cascade Lasers Pumped by Near-Infrared Light

by

Fariah Hayee

Student ID: 0412062208

A thesis submitted in partial fulfillment

for the degree of **Master of Science**

in the

Department of Electrical and Electronic Engineering

Bangladesh University of Engineering and Technology

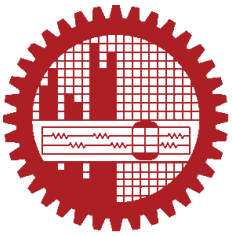

August, 2014

Declaration

It is hereby declared that this thesis or any part of it has not been submitted elsewhere for the award of any degree or diploma.

_____

(**Fariah Hayee**)

Approval Certificate

The thesis titled "Study of Dynamics of Mid-Infrared Quantum Cascade Lasers Pumped by Near-Infrared Light" submitted by Fariah Hayee, Student ID: 0412062208, Session: April 2012 has been accepted as satisfactory in partial fulfillment of the requirement for the degree of MASTER OF SCIENCE IN ELECTRICAL AND ELECTRONIC ENGINEERING on 09 August, 2014.

Board of Examiners

1._____ Chairman (Supervisor)

Dr. Muhammad Anisuzzaman Talukder
Associate Professor
Department of EEE, BUET
Dhaka-1205, Bangladesh

2._____ Member (Ex-Officio)

Dr. Taifur Ahmed Chowdhury
Professor and Head
Department of EEE, BUET
Dhaka-1205, Bangladesh

3._____ Member

Dr. Sharif Mohammad Mominuzzaman
Professor
Department of EEE, BUET
Dhaka-1205, Bangladesh

4._____ Member

Dr. Ishtiaque M. Syed
Associate Professor
Department of Physics
University of Dhaka

Abstract

Exploiting the intrinsic ultra-fast carrier relaxation life time in quantum cascade laser (QCL) nanostructures, all-optical modulation has recently gained large attraction due to its ability to circumvent the problem of parasitic effects associated with electrical modulation, and thus, resulting in a high modulation bandwidth. All-optical modulation of QCL offers an unique way to control intersubband transition through interband transition induced by injecting near-infrared (NIR) light into the cavity. In this thesis, we have modeled the changed carrier dynamics of a QCL due to photo-excited carriers created by NIR absorption. Electron-hole pairs are created when the NIR light excites an electron from valence to conduction band, thus, carrier densities of the conduction subbands increase. The spatial distribution of the carriers gives rise to additional band-bending, which changes the carrier transport in the QCL heterostructure significantly. These extra carriers also decrease the effective refractive index of the cavity, which shifts the photon modes to higher values. Using our transport model for GaAs/AlGaAs and InAlAs/InGaAs QCLs, we find that gain modulation depth of QCLs is proportional to injected NIR power. The emission wavelength of QCL also shows a blue shift, which varies proportionally with optical pumping power, thus enabling fast wavelength modulation by external light injection. Gain increases when the NIR light wavelength is close to QCL bandgap as the photoexcited carriers increases the population at the upper laser level. However, for NIR pumping energy larger than band-gap, gain decreases due to generation of hot-carriers. These high-k electrons eventually thermalize to injector ground but can not populate the upper lasing level because of the misalignment due to the band-bending created by excited carrier. NIR pulse duration significantly changes extra carrier generation and we achieve similar results for both pico-second and femto-second range pulses.

Acknowledgements

At first, I would like to convey my gratitude towards Almighty Allah for showering me with His blessing in every aspects of my life: be it professional or personal.

I am forever grateful to my thesis supervisor, Dr. Muhammad Anisuzzaman Talukder, whose constant guidance motivated me to complete this project successfully. He inspired me to work with this very idea as he also collaborated with his colleagues at UMBC who demonstrated the gain-quenching effects experimentally. During my thesis work, I used the "QCL Simulation Package" developed by him for solving the wavefunctions in quantum cascade lasers. We have had many successful discussions when I got stuck somewhere and his ideas and guidance helped me to find an alternate way in every one of these situations. I am grateful to have him as my undergraduate and graduate supervisor as he always inspires me to do more.

Next, I would like to thank my fellow researchers of "Nano-photonics Research Group" at BUET for their continuous support and help over the last year. I have had useful discussion with Golam Md. Imran Hossain and Saumya Biswas from time-to-time, and I wish them all the best. I also want to thank my colleagues and friends, Md. Shahadat Hasan Sohel, A.F.M. Saniul Haq, and Asif Ahmed for their help. am also very grateful to the project HEQEP CP-2091 for letting me use their resources for my simulations.

Finally, I would like to thank my loving husband; without his help I could not have achieved anything. He particularly helped during this thesis by providing occasional access to his remote server, when I needed an urgent computational facility at home. Also, my deepest gratitude is to my caring and supportive family who always encouraged me to excel at my professional life. Their support cannot be expressed in words, thus, I will conclude here on that note.

Contents

List of Figures

List of Acronyms

CW Continuous Wave

FWHM Full Width Half Maximum

NIR Near-Infrared

LO Longitudinal Optical

QCL Quantum Cascade Laser

ULL Upper Laser Level

LLL Lower Laser Level

IG Injector Ground

DFB Distributed Feedback

Chapter 1

Introduction

In most solid-state and gas lasers, lasing occurs when an electron makes a radiative transition from a higher energy state to a lower energy state of conduction band, thereby emitting a photon in the process. Here, population inversion is achieved by optical or electrical pumping [1]. By contrast, semiconductor diode lasers, including quantum well lasers, rely on transition between energy bands. Here, population inversion is achieved by forward biasing a junction formed by heavily doped n and p materials, so that conduction band electrons and valence band holes are injected into the active layer and they radiatively recombine across the band gap [2]. The band gap essentially determines the emission wavelength. In addition, since the population inversion is broadly distributed between two bands having dispersion with opposite curvature, in accordance with Pauli's principle, the resulting gain spectrum is relatively broad. These characteristics have significant effect on performance parameters of semiconductor lasers like peak gain, output intensity, linewidth of photoluminescence (PL) or electroluminescence (EL) spectrum [3].

In search of a narrow-linewidth wavelength tunable intersubband laser, the first step was laid by Kazarinov and Suris. In 1971, they proposed that optical gain could be obtained by using transitions between two dimensional states in a superlattice biased by an exter-

nal electric field [4]. In their scheme, Kazarinov and Suris [4] proposed that electrons tunnel from the ground state of a quantum well to the excited state of the neighboring well, emitting a photon in the process; which is often called photon-assisted tunneling. After emitting a photon, the electrons relax nonradiatively to the ground state and then tunnel into the excited state of the next stage to emit another photon. This process may be repeated many times. This structure introduced the concept of unipolar devices in which optical transitions could be completely engineered by careful choice of the thickness of the well and barrier materials, regardless of their energy gaps.

The structure that Kazarinov and Suris proposed, had two critical flaws because of which it hardly provided any optical gain. The first is the lack of reservoirs of electrons to inject carriers in each active region of the cascade. Without the reservoirs, the electrons are brought from contacts, as a result, the structure becomes electrically unstable due to the formation of space charge regions. The second is the lack of a region, where high energy electrons can relax to avoid the backfilling the ground state of laser transition [5]. The same electron reservoir that injects electrons into the active region can also act as a relaxation region by extracting the hot electrons from the ground state of the active region. After more than 15 years, overcoming the critical hindrances, Faist *et al.* demonstrated the first intersubband laser in 1994 at Bell Laboratories [3] .

This laser, referred to as quantum cascade laser (QCL), is unipolar. The electrons make transition between the conduction band states arising from the size quantization in semiconductor heterostructure. The joint density of states of these transitions and the corresponding gain spectrum are therefore narrow and symmetric [3]. The population inversion is achieved by engineering the lifetime between the two lasing levels and introducing a level below the lower lasing level at the longitudinal optical (LO) phonon resonance as shown in Fig. 1.1(a), so that the lower level is quickly depopulated by emitting LO phonons. Another fundamental feature is the multistage cascading scheme, where elec-

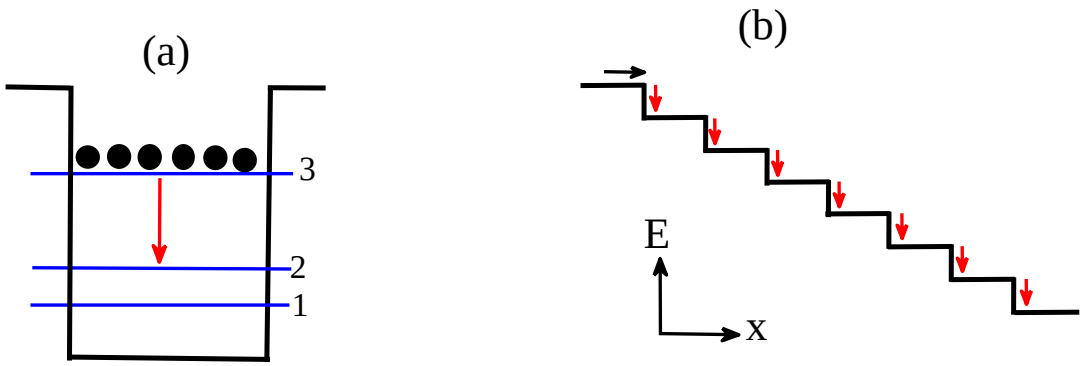

Figure 1.1: Schematic illustration of two unique features of quantum cascade laser: (a) unipolarity and (b) cascading. Here, the red arrow signifies photon emission and x denotes position along the growth axis and E is the energy of electron. The stair-case in terms of electron energy in (b) is formed by electron relaxing through intraband relaxation processes. Thus, the cascading scheme in (b) results in multiple photon emission from a single electron by providing it a energy relaxation staircase by emission of photon in active region and phonon in injector region.

trons are recycled from period to period, contributing each time to the gain and photon emission as illustrated schematically in FIg. 1.1(b). This leads to a quantum efficiency, $\eta \gg 1$ and thereby to a very high optical output power [5].

A very attractive feature of QCL is that the emission wavelength is not an intrinsic property of the semiconductor but a result of the design of the epitaxial layers. Also, the population inversion is not caused by some intrinsic physical property of the system, but must be designed by a suitable engineering of the wavefunctions. The ease of generating light at a design wavelength, tunable gain spectrum, and ultra-fast carrier dynamics make QCLs the most important semiconductor lasers that operate at room temperature in the mid-infrared range. The applications of QCLs are widespread, including medical and security imaging, environmental sensing, pollution monitoring, industrial process control, combustion control, breath analysis, and even free space communication.

One of the most attractive yet not fully explored features of QCLs is their intrinsic ultra-fast carrier relaxation time due to ultrafast phonon-electron interaction in the active region [5]. This ultra-fast carrier relaxation allows QCLs to follow changes in the injection current nearly immediately without relaxation oscillations, which is highly promising in high-speed communication applications, such as in free space optical links [6]. For free space optical links, near Infrared (NIR) sources are a mature technology. So, it will be advantageous if a mid-infrared QCL source can be modulated by a NIR source. Also, the fundamental limit of QCL modulation bandwidth is predicted to be around a tera-hertz, ehich is limited to 3 GHz when modulated by changing the electric current due to parasitic effects [7]. Even in optimized systems, parasitic effects limit the electrical modulation bandwidth to around 10 GHz.

One promising way to overcome the limiting parasitic effects is dto modulate QCLs optically. It has the potential to utilize the intrinsic speed of the carrier relaxation in the active region and can avoid the bottlenecks originating from the parasitic effects of electrical circuitry. If a mid-IR QCL output can be modulated by a NIR signal, it will allow us not only high-speed modulation beyond the electrical limit but also direct optical conversion of a NIR signal into a mid-IR signal. The switching of a QCL with a local oscillator would also allow for the retiming of an optical pulse train which has been subjected to random timing jitter during propagation, as well as reshaping and reamplifying it, i.e., so-called "3R" regeneration. With this in focus, Zervos et al. [8] demonstrated modulation of the mid-IR output of a standard GaAs/AlGaAs QCL by NIR light injection. They reported that the NIR control beam increases above-threshold QCL efficiency, as well as reduces the threshold current density. Therefore, a QCl biased just below threshold could produce a QCL output pulse sequence which is modulated by the NIR control beam. The spectral dependence of the amplitude of the switching effect shows sharp peaks at the same wavelength corresponding to interband photoluminescence spectrum, thus, sug-

gesting photo-excited electron-hole pairs initiating the modulation process.

However, the experimental observations of Zervos et al. [8] has directly been contradicted by the later experimentation by Sekine et al. [9], Chen et al. [6, 10] and Suchalkin et al. [11, 12]; where they reported the increase of threshold current and thereby decrease of QCL gain with external NIR injection. Chen et al. [6] also reported that the mid-IR optical modulation amplitude has a linear dependency on the NIR power when they excited a InAlAs/InGaAs QCL with a non-resonant NIR pulse of 1.51 eV (λ = 820 nm). As the excited pulse energy is larger than the bandgap, they attributed the reduction of gain to generation of hot-carriers. They postulated that, through very fast intraband relaxation, these hot carriers cool down by transferring energy to the previously thermalized electrons and effectively reduce the normally thermalized electron population at the bottom of the lasing levels. Since only the thermalized electrons near the subband edges contribute efficiently to the laser transition, the hot carriers cooling process reduces the population available for laser transition. As a result, the gain decreases, and so does the mid-IR QCL output power. However, this explanation does not justifies the gain increase as observed by Zervos et al. [8] and also directly contradicts the experimental results in Ref. [10], where it was reported that mid-IR QCL gain is enhanced with a 820 nm NIR pulse injection.

In addition to the gain modulation, Suchalkin et al. [11, 12] reported wavelength modulation of mid-IR QCLs due to NIR injection, which they attributed to the change in effective refractive index due to the extra carrier generated in the active region and the cladding layer. They demonstrated 0.3 cm^{-1} of continuous tuning with injected NIR energy. This feature has the potential to become one of the attractive mechanism to achieve tunable lasers. Two important tuning mechanisms for QCLs are the temperature tuning and Stark modulation. Frequency tuning of QCLs by temperature control changes effective refractive index using pump current modulation [13]. The bandwidth of the current

tuning for a room temperature operated device is strictly limited since high-performance CW QCLs must have efficient thermal packaging that prevents excessive heating and is estimated to be well below 25 MHz [13]. Tuning the emission frequency by Stark modulation of the optical transition energy either within the laser active region or in a separate passive section optically coupled with the laser waveguide is usually faster. Using the latter approach, it was possible to achieve over 10 GHz of continuous tuning of the laser emission line [14]. However, this approach results in a large increase in waveguide losses that prevent CW room-temperature operation of these lasers. Strong accompanying AM modulation of the laser emission is also an undesirable effect for FM data links.

The limitations of available methods of wavelength tuning of QCLs, as discussed above, can be mitigated if it can be tuned by changing the injected NIR pulse power, as experimental results indicate in Refs. [11, 12, 15, 16]. Wavelength modulation by creating electron-hole pairs by interband absorption combines advantages of continuous single mode tuning and high wavelength modulation speed; thus, is very promising. However, this optical tuning method needs detailed theoretically analysis to be useful in applications like wavelength conversion and free space optical communication. Gain modulation of the mid-IR QCL by NIR light is also of significance, as it will enable us to use QCLs for free space optical links. So, in our work, we want to establish a proper theoretical model for wavelength and gain modulation of mid-IR QCLs, when optically pumped by NIR light source. A detailed theoretical analysis is essential to resolve the apparent contradiction between the experimental results in Refs. [6, 8, 10–12], and thus, will play a very important role in establishing the amplitude and frequency modulation of mid-IR QCL by optically pumping of NIR light as a reliable technology.

In out work, we model the carrier transport in quantum cascade laser structures under external light injection, which excites interband transitions in the active materials. Carrier transport in the QCL heterostructure gives us a complete understanding about the device

operating conditions. The NIR excitation creates electron-hole pairs through interband absorption. Our approach is to model the interband absorption as a function of energy and gain an insight on the extra carrier energy distribution in the process. We use the so-called 8-band $\vec{k} \cdot \tilde{\mathbf{p}}$ method to solve the conduction and valence band electronic states. Interband absorption coefficient is calculated considering the high-k tail of the subbands to take hot-electron effect into consideration. From interband absorption spectra, we can calculate the excited electron-hole pair density distribution over different energy values, which enables us to correspond the energy the subbands and thus, the increase of carrier in the subbands. Our transport model takes into account the periodicity of QCL structures and solves time dependent carrier distribution in the subbands. We solve the transport equations for both before and after photo-excited carrier injection, and thus compare the gain and emission frequency of the mid-IR QCL.

Through our detailed analysis of carrier transport in QCL after NIR pulse injection, we establish a relationship between injected NIR power and gain and emission frequency modulation. With injected NIR pulse power increase, the modulation depth increases and the emission wavelength demonstrate a blue-shift. The modulation depth of mid-IR QCL output and the blue-shift of emission wavelength is a function of photo-excited carrier distribution over the subband, which in fact depends on NIR pulse duration, NIR wavelength, QCL structure material parameters and also QCL operating bias condition. Thus, our model can successfully predict the amplitude modulation and wavelength tuning behaviour when optically pumped by a NIR light.

The remainder of the thesis is organized as follows:

Chapter 2 introduces the theory of 8-band $\vec{k} \cdot \tilde{\mathbf{p}}$ method of zinc-blende materials, which is commonly used in mid-IR QCLs. It gives a compact Hamiltonian considering coupling between the three valence bands and the conduction bands. In this chapter, we also dis-

cuss the interband transitions and absorption coefficient calculation including the high-k electron tail.

Chapter 3 describes the scattering mechanisms contributing to lifetime broadening in the subbands of a QCL heterostructure. It also presents carrier transport calculations for QCLs. It introduces a model to calculate the carrier density in the energy levels of a QCL's active and injector regions. This model incorporates the carrier scattering and tunneling contributions under different design and operating conditions. Chapter 3 also presents the implementation of the carrier transport model for a QCL structure. We find the time evolution of the carrier densities at different energy levels for different operating electric fields.

Chapter 4 focuses on photoexcitation of carrier due to the NIR pulse injection. It models the extra carrier density in the different subbands and also presents the effect of extra carriers on lasing gain and wavelength. The extra carriers creates band-bending potential over the conduction and valence band edges, and thus, changes the electronic structure. The photoexcited carriers also reduces the effective refractive index in the active and cladding region. Chapter 4 gives a detailed model including all the effects from excited carriers and present the results for different QCLs operating in different biasing conditions and after injection of NIR pulse of different energy and power values.

Chapter 5 summarizes the results and draws conclusion on the findings.

Chapter 2

Calculation of Interband Absorption in Zinc Blende Nanostructures

2.1 Introduction

To model interband absorption in a semiconductor nanostructure, we need to consider the effects of multiple valence bands, i.e.,"heavy holes", "light holes" and "split off" bands, as these bands overlap in energy and even a weak electrical or optical potential can cause interband transitions. Therefore, single band effective mass equation cannot be used in this case, as it assumes constant effective mass for the conduction band (which is definitely not the case for valence bands) and also neglects the effect of coupling between conduction and valence bands. In this chapter, we will look into the multi-band $\vec{k} \cdot \tilde{\mathbf{p}}$ theory and how to calculate the 4-band Hamiltonian for zinc blende semiconductor nanostructures.

2.2 Solving Band Structure

In order to calculate interband absorption coefficient, the electronic structure, wave functions, and optical matrix elements are needed. These parameters can be obtained by using

8×8 envelop-function approximation (EFA) calculation. In this approach, the total wave function for both bound and continuum states is expanded as a linear combination of the products of the envelop functions and the zone-center ($\vec{k} = 0$) Bloch wave functions of the barrier and well materials [17]. The eight bands in the 8×8 EFA include the heavy-hole (**HH**), light-hole (**LH**), split-off (**SO**) and conduction (**C**) bands, which gives rise to eight-component wave-functions.

The use of the 8 band $\vec{k} \cdot \tilde{\mathbf{p}}$ theory allows us to incorporate in the first-order purterbation theory the coupling of the LH states to the C band. This provides an important contribution to the calculation of interband oscillator stregths for growth-direction polarized light.

2.2.1 Multi Band $\vec{k} \cdot \tilde{\mathbf{p}}$ Method

Within semiconductors, an electron is exposed to the periodic lattice potential which results in finite energy values for electrons, the energy bands. In general, electron wave functions need to satisfy the Schrödinger equation [17]

$$\frac{\hbar}{2m_0}\Delta^2\psi + V(\vec{r})\psi = E\psi, \tag{2.1}$$

where the potential V($\vec{r}$) represents the periodic semiconductor crystal. This equation is often written as

$$H\psi = E\psi \tag{2.2}$$

with H called the Hamiltonian. Within semiconductors, the solutions to the Schrödinger equation are so-called Bloch functions, which can be expressed as a linear combination of waves

$$\psi_n(\vec{k}, \vec{r}) = u_n(\vec{k}, \vec{r})\ \exp(i\vec{k}\vec{r}) \tag{2.3}$$

with the electron band index n. The most popular way to calculate the band structure $E(\vec{k})$ near the Γ point is the so-called $\vec{k} \cdot \tilde{\mathbf{p}}$ method [18]. This model introduces the Bloch function from Eq. (2.3) into the single-electron Schrödinger equation

$$\left[-\frac{\tilde{\mathbf{p}}\cdot\tilde{\mathbf{p}}}{2m_0} + V(\vec{r}) + \frac{\hbar}{2m_0}\right] u_n(\vec{k},\vec{r}) = \left[E_n(\vec{k}) - \frac{\hbar^2 k^2}{2m_0} u_n(\vec{k},\vec{r})\right]. \tag{2.4}$$

The momentum operator $\tilde{\mathbf{p}}$ stands for $-i\hbar\Delta$. The functions $u_n(\vec{k},\vec{r})$ constructed as linear expansions given by:

$$u_n(\vec{k},\vec{r}) = \sum a_{nm} u_{m0}(\vec{r}). \tag{2.5}$$

The basis vectors often used for the multiple valence bands are:

Heavy-Hole State:	$\lvert\frac{3}{2},\pm\frac{3}{2}\rangle$
Light-Hole State:	$\lvert\frac{3}{2},\pm\frac{1}{2}\rangle$
Split-Off State:	$\lvert\frac{1}{2},\pm\frac{1}{2}\rangle$

2.2.1.1 Three- and Four-Band Model (Zinc Blende Material)

If we consider the conduction band well separated from the valence bands, we can use the three band $\vec{k} \cdot \tilde{\mathbf{p}}$ model which will give us a 3×3 Hamiltonian, which will eventually result in a 6×6 Hamiltonian including spin-degeneracy.

The Hamiltonian H from the Burt theory, with no spin-orbit interaction, is shown in Table 2.1.

Table 2.1: Burt Hamiltonian elements considering 4 bands and without spin degeneracy

$E_{CB} + \frac{\hbar^2(\hat{k}_x^2+\hat{k}_y^2+\hat{k}_z^2)}{2m_0} + \hat{k}_x \acute{A} \hat{k}_x + \hat{k}_y \acute{A} \hat{k}_y + \hat{k}_z \acute{A} \hat{k}_z$	$\frac{i\hbar P}{m_0}\hat{k}_x + \hat{k}_y \frac{B}{2}\hat{k}_z + \hat{k}_z \frac{B}{2}\hat{k}_y$	$\frac{i\hbar P}{m_0}\hat{k}_y + \hat{k}_z \frac{B}{2}\hat{k}_x + \hat{k}_x \frac{B}{2}\hat{k}_z$	$\frac{i\hbar P}{m_0}\hat{k}_z + \hat{k}_x \frac{B}{2}\hat{k}_y + \hat{k}_y \frac{B}{2}\hat{k}_x$
$\frac{i\hbar P}{m_0}\hat{k}_x + \hat{k}_y \frac{B}{2}\hat{k}_z + \hat{k}_z \frac{B}{2}\hat{k}_y$	$E_{VB} + \frac{\hbar^2(\hat{k}_x^2+\hat{k}_y^2+\hat{k}_z^2)}{2m_0} + \hat{k}_x(\acute{F} + 2G)\hat{k}_x + \hat{k}_y(H_1 + H_2)\hat{k}_y + \hat{k}_z(H_1 + H_2)\hat{k}_z$	$\hat{k}_x(\acute{F} - G)\hat{k}_y + \hat{k}_y(H_1 - H_2)\hat{k}_x$	$\hat{k}_x(\acute{F} - G)\hat{k}_z + \hat{k}_z(H_1 - H_2)\hat{k}_x$
$\frac{i\hbar P}{m_0}\hat{k}_y + \hat{k}_z \frac{B}{2}\hat{k}_x + \hat{k}_x \frac{B}{2}\hat{k}_z$	$\hat{k}_y(\acute{F} - G)\hat{k}_x + \hat{k}_x(H_1 - H_2)\hat{k}_y$	$E_{VB} + \frac{\hbar^2(\hat{k}_x^2+\hat{k}_y^2+\hat{k}_z^2)}{2m_0} + \hat{k}_y(\acute{F} + 2G)\hat{k}_y + \hat{k}_x(H_1 + H_2)\hat{k}_x + \hat{k}_z(H_1 + H_2)\hat{k}_z$	$\hat{k}_y(\acute{F} - G)\hat{k}_z + \hat{k}_z(H_1 - H_2)\hat{k}_y$
$\frac{i\hbar P}{m_0}\hat{k}_z + \hat{k}_x \frac{B}{2}\hat{k}_y + \hat{k}_y \frac{B}{2}\hat{k}_x$	$\hat{k}_z(\acute{F} - G)\hat{k}_x + \hat{k}_x(H_1 - H_2)\hat{k}_z$	$\hat{k}_z(\acute{F} - G)\hat{k}_y + \hat{k}_y(H_1 - H_2)\hat{k}_z$	$E_{VB} + \frac{\hbar^2(\hat{k}_x^2+\hat{k}_y^2+\hat{k}_z^2)}{2m_0} + \hat{k}_z(\acute{F} + 2G)\hat{k}_z + \hat{k}_x(H_1 + H_2)\hat{k}_x + \hat{k}_y(H_1 + H_2)\hat{k}_y$

Including the conduction band coupling, the 8×8 Hamiltonian H has the form [19]:

$$\begin{pmatrix} H_{1,1} & H_{1,2} & H_{1,3} & H_{1,4} & 0 & 0 & 0 & 0 \\ H_{2,1} & H_{2,2} & H_{2,3} - i\frac{\Delta}{3} & H_{2,4} & 0 & 0 & 0 & \frac{\Delta}{3} \\ H_{3,1} & H_{3,2} + i\frac{\Delta}{3} & H_{3,3} & H_{3,4} & 0 & 0 & 0 & -i\frac{\Delta}{3} \\ H_{4,1} & H_{4,2} & H_{4,3} & H_{4,4} & 0 & -\frac{\Delta}{3} & i\frac{\Delta}{3} & 0 \\ 0 & 0 & 0 & 0 & H_{1,1} & H_{1,2} & H_{1,3} & H_{1,4} \\ 0 & 0 & 0 & -\frac{\Delta}{3} & H_{2,1} & H_{2,2} & H_{2,3} + i\frac{\Delta}{3} & H_{2,4} \\ 0 & 0 & 0 & -i\frac{\Delta}{3} & H_{3,1} & H_{3,2} - i\frac{\Delta}{3} & H_{3,3} & H_{3,4} \\ 0 & \frac{\Delta}{3} & i\frac{\Delta}{3} & 0 & H_{4,1} & H_{4,2} & H_{4,3} & H_{4,4} \end{pmatrix} \tag{2.6}$$

.

At each point z, the eigenvalue problem is written as:

$$(H) \begin{pmatrix} F_1(z) \\ F_2(z) \\ F_3(z) \\ F_4(z) \\ F_5(z) \\ F_6(z) \\ F_7(z) \\ F_8(z) \end{pmatrix} = E \begin{pmatrix} F_1(z) \\ F_2(z) \\ F_3(z) \\ F_4(z) \\ F_5(z) \\ F_6(z) \\ F_7(z) \\ F_8(z) \end{pmatrix} \tag{2.7}$$

Thus, for each grid point, there will be eight equations as there are eight basis vectors in play.

For a nanostructure grown in z direction, the periodicity at the other two directions x and y is preserved. Thus, energy will be quantized only in the z direction. So, the momentum

operators in the Table 2.1 become:

$$\hat{k}_x = k_x, \quad \hat{k}_y = k_y, \quad \text{and} \quad \hat{k}_z = -i\delta/\delta z \tag{2.8}$$

Now, The operator $\hat{k}_z = -i\delta/\delta z$ will generate four kinds of terms: (a) terms with no derivative operators $H_{ij}^{(a)}$, (b) terms with the derivative operator on the right $H_{ij}^{(b)}$, (c) terms with the derivative operator on the left $H_{ij}^{(c)}$, and (d) terms sandwiched between derivative operators $H_{ij}^{(d)}$.

Eq (2.6), the hamiltonian elements are listed in the table below: We use the notation

$$H_{ij}^{(a)} \equiv h_{ij}^{(a)} \tag{2.9a}$$

$$H_{ij}^{(b)} \equiv h_{ij}^{(b)} \frac{\delta}{\delta \mathrm{z}} \tag{2.9b}$$

$$H_{ij}^{(c)} \equiv \frac{\delta}{\delta \mathrm{z}} h_{ij}^{(c)} \tag{2.9c}$$

$$H_{ij}^{(d)} \equiv \frac{\delta}{\delta \mathrm{z}} h_{ij}^{(d)} \frac{\delta}{\delta \mathrm{z}}. \tag{2.9d}$$

The Hamiltonian of type (a) are

$$h^{(a)}_{1,1} = E_{CB} + \frac{\hbar^2(k_x^2 + k_y^2)}{2m_0} + \acute{A}(k_x^2 + k_y^2), \tag{2.10a}$$

$$h^{(a)}_{1,2} = \frac{i\hbar P}{m_0}k_x, \tag{2.10b}$$

$$h^{(a)}_{1,3} = \frac{i\hbar P}{m_0}k_y, \tag{2.10c}$$

$$h^{(a)}_{1,4} = Bk_xk_y, \tag{2.10d}$$

$$h^{(a)}_{2,1} = \frac{i\hbar P}{m_0}k_x, \tag{2.10e}$$

$$h^{(a)}_{2,2} = E_{VB} + \frac{\hbar^2(k_x^2 + k_y^2)}{2m_0} + (\acute{F} + 2G)k_x^2 + (H_1 + H_2)k_y^2, \tag{2.10f}$$

$$h^{(a)}_{2,3} = (\acute{F} - G)k_xk_y + (H_1 + H_2)k_xk_y, \tag{2.10g}$$

$$h^{(a)}_{3,1} = \frac{i\hbar P}{m_0}k_y, \tag{2.10h}$$

$$h^{(a)}_{3,2} = (\acute{F} - G)k_xk_y + (H_1 - H_2)k_xk_y, \tag{2.10i}$$

$$h^{(a)}_{3,3} = E_{VB} + \frac{\hbar^2(k_x^2 + k_y^2)}{2m_0} + (\acute{F} + 2G)k_y^2 + (H_1 + H_2)k_x^2, \tag{2.10j}$$

$$h^{(a)}_{4,1} = Bk_xk_y, \tag{2.10k}$$

$$h^{(a)}_{4,4} = E_{VB} + \frac{\hbar^2(k_x^2 + k_y^2)}{2m_0} + (H_1 + H_2)k_x^2 + (H_1 + H_2)k_y^2. \tag{2.10l}$$

The Hamiltonian elements of type (b) are

$$h_{1,2}^{(b)} = -ik_y\frac{B}{2}, \tag{2.11a}$$

$$h_{1,3}^{(b)} = -ik_x\frac{B}{2}, \tag{2.11b}$$

$$h_{1,4}^{(b)} = \frac{\hbar P}{m_0}, \tag{2.11c}$$

$$h_{2,1}^{(b)} = -ik_y\frac{B}{2}, \tag{2.11d}$$

$$h_{2,4}^{(b)} = ik_x(\acute{F} - G), \tag{2.11e}$$

$$h_{3,1}^{(b)} = -ik_x\frac{B}{2} \tag{2.11f}$$

$$h_{3,4}^{(b)} = ik_y(\acute{F} - G), \tag{2.11g}$$

$$h_{4,1}^{(b)} = -\frac{\hbar P}{m_0}, \tag{2.11h}$$

$$h_{4,2}^{(b)} = -ik_x(H_1 - H_2), \tag{2.11i}$$

$$h_{4,2}^{(b)} = -ik_y(H_1 - H_2). \tag{2.11j}$$

The Hamiltonian elements of type (c) are

$$h_{1,2}^{(c)} = -i\frac{B}{2}k_y, \tag{2.12a}$$

$$h_{1,3}^{(c)} = -i\frac{B}{2}k_x, \tag{2.12b}$$

$$h_{2,1}^{(c)} = -i\frac{B}{2}k_y, \tag{2.12c}$$

$$h_{2,4}^{(c)} = -i(H_1 - H_2)k_x, \tag{2.12d}$$

$$h_{3,1}^{(c)} = -i\frac{B}{2}k_x, \tag{2.12e}$$

$$h_{3,4}^{(c)} = -i(H_1 - H_2)k_y, \tag{2.12f}$$

$$h_{4,2}^{(c)} = -i(\acute{F} - G)k_x, \tag{2.12g}$$

$$h_{4,3}^{(c)} = -i(\acute{F} - G)k_y. \tag{2.12h}$$

The Hamiltonian elements of type (d) are

$$h^{(d)}_{1,1} = -\left(\frac{\hbar^2}{2m_0} + \acute{A}\right) \tag{2.13a}$$

$$h^{(d)}_{2,2} = \left(\frac{\hbar^2}{2m_0} + H_1 + H_2\right) \tag{2.13b}$$

$$h^{(d)}_{3,4} = \left(\frac{\hbar^2}{2m_0} + H_1 + H_2\right) \tag{2.13c}$$

$$h^{(d)}_{4,4} = \left(\frac{\hbar^2}{2m_0} + \acute{F} + 2G.\right) \tag{2.13d}$$

2.2.1.2 Applying Finite Difference Method

We have applied finite difference method (FDM) to solve the differential equations. Let us take n number of grid point along the growth direction z. With the notation $F_{j,n} \equiv F_j(z_n)$, $h_{i,j,n} \equiv h_{i,j}(z_n)$, the derivatives are calculated with a central difference scheme, which is equally applicable for non-uniform grid. The central difference equation for n^{th} point is

$$\frac{\delta F_{j,n}}{\delta z} = F_{j,n-1}A_n + F_{j,n}B_n + F_{j,n+1}C_n, \tag{2.14}$$

where

$$A_n = \frac{-\Delta z_n}{\Delta z_{n-1}(\Delta z_{n-1} + \Delta z_n)} \tag{2.15a}$$

$$B_n = \frac{\Delta z_n - \Delta z_{n-1}}{\Delta z_{n-1}\Delta z_n} \tag{2.15b}$$

$$C_n = \frac{\Delta z_n}{\Delta z_{n-1}(\Delta z_{n-1} + \Delta z_n)} \tag{2.15c}$$

and $\Delta z = z_{n+1} - z_n$. The terms sandwiched between derivatives are expanded as

$$\begin{aligned}
\frac{\partial}{\partial z}\left(h^{(d)}_{i,j,n}\frac{\partial F_{j,n}}{\partial z}\right) &= h^{(d)}_{i,j,n-1/2}\frac{\partial F_{j,n-1/2}}{\partial z}2A_n + h^{(d)}_{i,j,n}\frac{\partial F_{j,n}}{\partial z}2B_n + h^{(d)}_{i,j,n+1/2}\frac{\partial F_{j,n+1/2}}{\partial z}2C_n \\
&= \frac{h^{(d)}_{i,j,n-1} + h^{(d)}_{i,j,n}}{2}\frac{F_{j,n} - F_{j,n-1}}{\Delta z_{n-1}}2A_n + h^{(d)}_{i,j,n}\frac{F_{j,n+1} - F_{j,n-1}}{\Delta z_{n-1} + \Delta z_n}2B_n \\
&+ \frac{h^{(d)}_{i,j,n+1} + h^{(d)}_{i,j,n}}{2}\frac{F_{j,n+1} - F_{j,n}}{\Delta z_n}2C_n.
\end{aligned} \tag{2.16}$$

The contribution of the four terms are added in the eigenvalue problem

$$
\begin{aligned}
h^{(a)}_{i,j,n} F_{j,n} &= h^{(a)}_{i,j,n} F_{j,n}, && (2.17)\\
h^{(b)}_{i,j,n} \frac{\partial}{\partial z} F_{j,n} &= F_{j,n-1} A_n h^{(b)}_{i,j,n} + F_{j,n} B_n h^{(b)}_{i,j,n} + F_{j,n} C_n h^{(b)}_{i,j,n}, && (2.18)\\
\frac{\partial}{\partial z} h^{(c)}_{i,j,n} F_{j,n} &= F_{j,n-1} h^{(c)}_{i,j,n-1} A_n + F_{j,n} h^{(c)}_{i,j,n-1} B_n + F_{j,n+1} h^{(c)}_{i,j,n+1} C_n, && (2.19)\\
\frac{\partial}{\partial z} h^{(d)}_{i,j,n} \frac{\partial}{\partial z} F_{j,n} &= F_{j,n-1} \left(-\frac{h^{(d)}_{i,j,n-1} + h^{(d)}_{i,j,n}}{\Delta z_{n-1}} A_n - \frac{h^{(d)}_{i,j,n}}{\Delta z_{n-1} + \Delta z_n} 2B_n \right) \\
&+ F_{j,n} \left(\frac{h^{(d)}_{i,j,n-1} + h^{(d)}_{i,j,n}}{\Delta z_{n-1}} A_n - \frac{h^{(d)}_{i,j,n} + h^{(d)}_{i,j,n+1}}{\Delta z_n} C_n \right) \\
&+ F_{j,n+1} \left(\frac{h^{(d)}_{i,j,n+1} + h^{(d)}_{i,j,n}}{\Delta z_n} A_n + \frac{h^{(d)}_{i,j,n}}{\Delta z_{n-1} + \Delta z_n} 2B_n. \right) && (2.20)
\end{aligned}
$$

When spin is included we have additional terms $h_{i+4,j+4,n} = h_{i,j,n}$. The spin-orbit Hamiltonian will give an extra contribution of type (a).

2.2.1.3 The Hamiltonian Structure: Formation of the Sparse Matrix

The discretization of the eight folded Eq. (2.7) obtained for every grid point will produce a matrix of dimension $8N_z$, where N_z is the number of grid points. The indices of the matrix elements are obtained as $I = i + 8(n-1)$, $J = j + 8(n-1)$, where n is the index of the grid point, and i, and j are indices for the 8 bands. The first step in writing the sparse matrix is the identification of the non-zero elements. The structure of the non-zero 8×8

blocks is

1	2	0	0	…	…	0	0
3	4	5	0	…	…	0	0
0	6	7	8	…	…	0	0
0	0	9	10	…	…	0	0
0	0	0	13	…	…	0	0
0	0	0	0	…	…	0	0
0	0	0	0	…	…	$K-3$	$K-2$
0	0	0	0	…	…	$K-1$	K

(2.21)

and the number of non-zero blocks is $K = 4 + 3(N_z - 2)$. The non-zero elements in the non-diagonal blocks are

1	2	3	4	0	0	0	0
5	6	7	8	0	0	0	0
9	10	11	12	0	0	0	0
13	14	15	16	0	0	0	0
0	0	0	0	17	18	19	20
0	0	0	0	21	22	23	24
0	0	0	0	25	26	27	28
0	0	0	0	29	30	31	32

(2.22)

The non-zero elements in the diagonal blocks are:

1	2	3	4	0	0	0	0
5	6	7	8	0	0	0	33
9	10	11	12	0	0	0	34
13	14	15	16	0	35	36	0
0	0	0	0	17	18	19	20
0	0	0	37	21	22	23	24
0	0	0	38	25	26	27	28
0	39	40	0	29	30	31	32

(2.23)

Eight extra non-zero elements appear due to the spin-orbit interaction.

Once the non-zero elements have been identified, they have to be numbered, for the easy handling of the sparse matrix. The elements are numbered by running the sequence of non-zero blocks, in the order shown. In each block the non-zero elements are numbered in the order shown in Eq. (2.23). The total number of non-zero elements is $144+104(N_z-2)$.

2.2.1.4 Simulation Setup

Boundary Condition:

There are three types of boundary conditions that can be imposed, such as

- 1)Neumann Boundary Condition
- 2)Dirichlet Boundary Condition
- 3)Periodic Boundary Condition

While solving the eigen-value problem for a periodic structure like quantum cascade laser, we used the periodic boundary condition.

Material Parameters:

The material parameters needed for this theoretical modeling is given in Table 2.2.1.4 [19]

Table 2.2: 8-band Kane parameter for GaAs, $Al_{0.3}Ga_{0.7}As$, and AlAs

Parameters	GaAs (well)	$Al_{0.3}Ga_{0.7}As$ (barrier)	AlAs (barrier)
E_{CB} [eV]	1.519	1.74346	2.2672
E_{VB} [eV]	-0.114333333	-0.257773333	-0.592466667
Δ [eV]	0.343	0.3244	0.281
$\acute{A}$ [eV Å^2]	-10.5081159	-13.5189727	-13.0507385
B [eV Å^2]	0.0	0.0	0.0
$\acute{F}$ [eV Å^2]	21.7239273	14.3009371	11.9969319
G [eV Å^2]	-4.2443222	-4.3692897	-4.66088055
H_1 [eV Å^2]	-15.0189573	-13.1764490	-8.87726296
H_2 [eV Å^2]	0.0	0.0	0.0
$\frac{\hbar P}{m_0}$ [eV Å]	10.4750915	10.4750915	10.4750915

2.3 Inter-band Absorption

2.3.1 Fermi's Golden Rule

Optical gain in semiconductors is caused by photon-induced transitions of electrons from the conduction band (CB) to the valence band (VB). Thus, in order to understand optical gain, we need to characterize electron-photon interactions in the crystal. To examine the interaction, we represent the photon classically by an electromagnetic wave. The wave's interaction with the electron enters into the Schroedinger equation through the vector potential which can be expressed as

$$\mathbf{A}(\mathbf{r},t) \;=\; \hat{e}\,\mathrm{Re}[A(\mathbf{r})e^{-j\omega t}] \;=\; \hat{e}\frac{1}{2}[A(r)e^{-j\omega t} \;+\; A^{*}(r)e^{j\omega t}], \tag{2.24}$$

where $\hat{e}$ is the unit polarization vector in the direction of $\mathbf{A}$, and ω is the angular frequency of photon wave. The Schrödinger equation is now modified by the substitution

$$\mathbf{p^2} \rightarrow (\mathbf{p} + e\mathbf{A})^2 \approx \mathbf{p^2} \ + \ 2e\mathbf{A}.\mathbf{p}. \tag{2.25}$$

Substituting Eq. (2.25) into Eq. (2.1), we can write the new Hamiltonian as

$$H \ = \ H_0 \ + \ [\acute{H}(\mathbf{r})e^{-j\omega t} + \text{h.c.}], \tag{2.26}$$

where, $\acute{H}(\mathbf{r}) = \frac{e}{2m_0}A(\mathbf{r})\hat{e}.\mathbf{p}$ and h.c. stands for Hermitian conjugate.

In quantifying the gain, we need to know the number of transitions that will occur per second in the crystal in response to a given flux of photons in a given optical mode. The transition rate can be expressed (in units of s^{-1}) as

$$W_{h\rightarrow e} = \frac{2\pi}{\hbar}|H_{he}|^2 \ \delta(E_h - E_e - \hbar\omega), \tag{2.27}$$

where

$$\acute{H}_{he} \ \equiv \ \langle\psi_e|\acute{H}(\mathbf{r})|\psi_h\rangle \ = \ \int_V \psi_e^*\acute{H}(\mathbf{r})\psi_h d^3\mathbf{r}. \tag{2.28}$$

2.3.2 Absorption Co-efficient

Equation (2.27) allows us to quantify the number of upward transitions from valence band to conduction band, occurring per second per unit volume in response to a flux of incoming photons in a given optical mode. Upward transitions or absorption of photons will also occur in response to the photon flux. Each downward transition generates a new photon, while each upward transition absorbs one. If the number of downward transitions per second exceeds the number of upward transitions, there will be a net generation of photons, and optical gain can be achieved. If we assume an electromagnetic wave propagating in the z direction, then the net decrease in photon flux per unit length along

the z direction can simply be written as

$$\frac{d\Phi}{dz} = W_{v\to c} - W_{c\to v}, \tag{2.29}$$

where Φ is the photon flux (in units of $s^{-1}m^{-2}$). The optical absorption α of the material is usually defined as the fractional decrease in photons per unit length, or simply

$$\alpha = \frac{1}{\Phi}\frac{d\Phi}{dz}. \tag{2.30}$$

Substituting the transition rate given in Eq. (2.27) in Eq. (2.29), we can write the expression for gain as

$$\alpha(\hbar\omega) = -\left(\frac{1}{\hbar\omega}\right)\frac{\pi e^2\hbar}{\epsilon_0 c m_0^2}\frac{n_{eff}^2}{n^2}|M.E|^2\rho_{red}(E_{eh}-E_g)(f_v-f_c). \tag{2.31}$$

2.4 Summary

We have presented the Burt formalism of eight-band $\vec{k}\cdot\tilde{\mathbf{p}}$ method to calculate the valence and conduction band electronic band structures. The effect of spin degeracy has been taken into account. We have also calculated the interband absorption coefficient for a QCL heterostucture. 8-band $\vec{k}\cdot\tilde{\mathbf{p}}$ method is advantageous for calculating interband absorption spectra as it can easily calculate the electronic band structure for high-k values which is essential for calculating interband absorption.

Chapter 3

Intersubband Gain in QCL with NIR Light Injection

3.1 Introduction

QCL structures have ultrafast carrier relaxation time due to ultrafast phonon-electron interaction in the active region [5], which allows the QCL to follow changes in the injection current nearly immediately without relaxation oscillations and is highly promising in high-speed communication applications [6]. The fundamental limit of QCL modulation bandwidth was predicted to be around terahertz, but the electrical modulation is typically limited to around 3 GHz for standard QCLs due to the electrical parasitic effects [7].

One promising way to overcome these restrictions is direct all-optical modulation. It has the potential to utilize the intrinsic speed of the carrier relaxation in the active region and can avoid the bottlenecks originating from the electrical circuitry. Several research groups have carried out experiments to modulate mid-IR QCL output with NIR pump pulse injection [6, 8–12, 15, 16]. However, a detailed theoretical analysis to understand the underlying physics is yet to be done.

The experimental observations indicate that NIR light excites carriers from valence band to conduction band, thereby creating electron-hole pairs in the active region and cladding layers. Excitonic effects can be neglected here as the QCL operates in room temperature [20]. However, spatial distribution of excited electronscreate a considerable Poisson potential, which can result in significant bending in the conduction band energy profile. As a result, the confined electron states in the quantum heterostructure will change in energy and spatial distribution. The new wavefunctions and energy values will have significant effect on the carrier transport, which will depend on the applied bias, the properties of the NIR light, and the material system used for the QCL.

In order to compare the performance of a QCL with and without NIR pulse injection, it is important to understand the carrier transport mechanism through the structure. Performance parameters like EL linewidth and laser gain has direct dependence on population inversion between the two lasing subbands, whereas parameters like gain recovery time has inherent linkage to carrier transport. Thus, to understand and model the various non-radiative scattering mechanisms contributing to finite subband lifetimes will lead to basic understanding of carrier transport, which will also contribute to understanding the effect of NIR pulse on QCL performance.

In general, carrier transport through a QCL is a complicated process as electrons may move due to both coherent and incoherent mechanisms [21–23]. In a typical QCL structure, carriers move within an injector region and within an active region principally by scattering, while carriers move between the injector and active regions principally by tunneling. Scattering mechanisms include electron-Longitudinal Optical (LO) phonon scattering, electron-electron scattering, electron-acoustic phonon scattering, electron-interface roughness scattering, and electron-impurity ions scattering. For the usual energy spacing between the subbands in a QCL, electron scattering due to interaction with LO phonons is the dominant scattering mechanism in the intersubband transitions

[24, 25]. However, electron-electron scattering may become significant if the subbands have an energy spacing that is much smaller than the LO phonon resonance energy [26]. Electron-electron scattering is also the dominant scattering mechanism in transitions that occur within a single subband [26, 27].

In this chapter, at first we will discuss a general model of carrier transport in QCL heterostructures. We will calculate time-resolved carrier densities at each of the levels so that a clear illustration of the effects of the underlying physical processes can be obtained. Then, we will introduce the carrier transport model with NIR light injection. We will calculate the photo-excited carrier density distribution, generated by the NIR pulse and we find that the extra carrier density can be comparable to that of the QCL structure's own doping density depending upon the duration of the pulse. Thus, we cannot neglect the charge carriers' (electron in CB and hole in VB) effect on band-edge potential. We calculate the electronic states using self-consistent Schrödinger-Poisson solver. The extra carrier also decreases the effective refractive index, which we will also add into our model.

The remainder of this chapter is organized as follows: Sec. 3.2 introduces the parameters necessary for calculating intersubband gain. Section 3.3 explains a carrier transport model for a cascaded structure including the effects of coherent and non-coherent mechanisms. Section 3.4 discusses the inclusion of photo-generated carrier to the QCL transport model. Finally, in Sec. 3.5 and 3.6, the effects of photo generated carriers on electronic band structure and effective refractive index are discussed, respectively.

3.2 Performance Parameters

In order to study the effects of NIR pulse injection in mid-IR QCLs, we focus on two performance parameters: Gain and emission wavelength. Emission wavelength is de-

termined by the sustainable mode in the cavity that overcomes the cavity losses and is nearest to the peak of EL spectrum.

3.2.1 Intersubband Gain

The peak modal gain between two sub-bands $|i\rangle$ and $|j\rangle$ assuming Lorentzian lineshape is given by [28]

$$G_m = G_p \Gamma, \tag{3.1}$$

where G_p is the peak material gain between sub-bands $|i\rangle$ and $|j\rangle$ and Γ is the overlap factor of the modes. The parameter $mathrmG_p$ is given by

$$G_m = \frac{4\pi q^2}{\epsilon_o n \lambda_o} \frac{z_{ij}^2}{2\gamma_{ij} L_p} (N_i - N_j). \tag{3.2}$$

Here, q is the charge of an electron, ϵ_o is the permittivity of laser medium, n is the effective refractive index, λ_o is the photon wavelength, $2\gamma_{ij}$ is the FWHM linewidth of QCL, L_p is the length of active region of QCL, z_{ij} is the dipole matrix element, N_i is the sheet electron density in the upper lasing level $|i\rangle$ and N_j is the sheet electron density in the lower lasing level $|j\rangle$.

3.2.2 Modes

Modes of quantum cascade lasers depend on the length and effective refractive index of the cavity. The two mirrors of the laser form a resonant cavity and standing wave patterns are set up between the mirrors. The resonant frequencies of the QCL are given by [1]

$$f = m \frac{c}{2nL}, \tag{3.3}$$

where m is an integer, c is the speed of light and L is the cavity length of QCL. Each value of m satisfying Eq. 3.3 defines an axial (or longitudinal) mode of the cavity. While

any integer m gives a possible axial cavity mode, only those falling within the gain curve and receiving more gain than loss can actually oscillate. In a homogeneously broadened gain medium as in QCLs, the mode that first experiences gain greater than loss will be supported by the cavity.

3.3 Carrier Transport Model

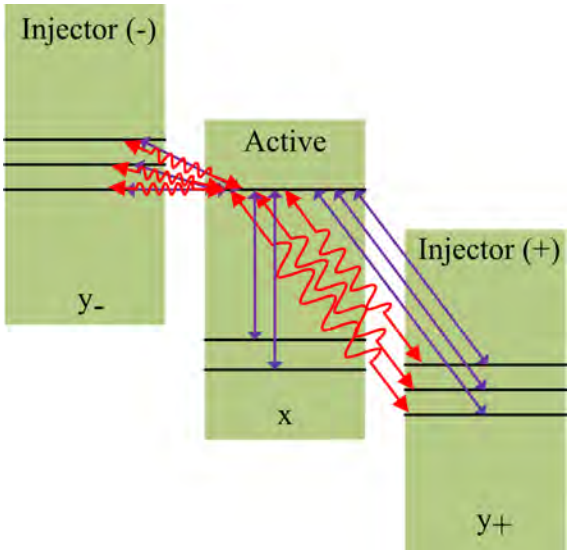

Figure 3.1: Schematic illustration of the carrier transport model for one and half periods [29]. In the model, it is assumed that transitions between the injector and collector regions are negligible [26]. The straight arrows represent incoherent scattering mechanisms. The wavy arrows indicate coherent carrier transport. As carrier transport can be in either direction, we use double arrows.

A detailed theoretical study incorporating coherent and non-coherent mechanisms is necessary for correctly calculating the carrier densities in the different subbands [29]. Various approaches have been discussed by the authors in Refs. [22, 26, 30–32]. We write the density equations folowing the approach discussed in Ref. [23, 29]. In Fig. 3.1, we show an example how the carrier density equations are formulated in the model.

The density equations are written following Ref. [29] as

$$\frac{dn_{A,x}}{dt} = \sum_{x'\neq x}\frac{n_{A,x}}{s_{x'x}} + \sum_{y^-}\frac{n_{I,y^-}}{s_{y^-x}} + \sum_{y^+}\frac{n_{A,y^+}}{s_{y^+x}} - \sum_{y^-}\frac{n_{A,x}}{s_{xy^-}} - \sum_{x'\neq x}\frac{n_{A,x}}{s_{xx'}} - \sum_{y^+}\frac{n_{A,x}}{s_{xy^+}}$$
$$- i\frac{\Delta_{0,xy^+}}{2\hbar}\sum_{y^+}\left(C_{xy^+} - C^*_{xy^+}\right) + i\frac{\Delta_{0,y^-x}}{2\hbar}\sum_{y^+}\left(C_{y^-x} - C^*_{y^-x}\right), \quad (3.4)$$

$$\frac{dn_{I,y^-}}{dt} = \sum_{y^{-\prime}\neq y^-}\frac{n_{I,y^{-\prime}}}{s_{y^{-\prime}y^-}} + \sum_{x}\frac{n_{A,x}}{s_{xy^+}} + \sum_{x}\frac{n_{A,x}}{s_{xy^-}} - \sum_{x}\frac{n_{I,y^-}}{s_{y^-x}} - \sum_{x}\frac{n_{I,y^+}}{s_{y^+x}} - \sum_{y^{-\prime}\neq y^-}\frac{n_{I,y^-}}{s_{y^-y^{-\prime}}}$$
$$- i\frac{\Delta_{0,y^-x}}{2\hbar}\sum_{x}\left(C_{y^-x} - C^*_{y^-x}\right) + i\frac{\Delta_{0,xy^+}}{2\hbar}\sum_{y^+}\left(C_{xy^+} - C^*_{xy^+}\right), \quad (3.5)$$

$$\frac{dn_{I,y^+}}{dt} = \sum_{y^{+\prime}\neq y^+}\frac{n_{I,y^{+\prime}}}{s_{y^{+\prime}y^+}} + \sum_{x}\frac{n_{A,x}}{s_{xy^+}} + \sum_{x}\frac{n_{A,x}}{s_{xy^-}} - \sum_{x}\frac{n_{I,y^-}}{s_{y^-x}} - \sum_{x}\frac{n_{I,y^+}}{s_{y^+x}} - \sum_{y^{+\prime}\neq y^+}\frac{n_{I,y^+}}{s_{y^+y^{+\prime}}}$$
$$- i\frac{\Delta_{0,y^-x}}{2\hbar}\sum_{x}\left(C_{y^-x} - C^*_{y^-x}\right) + i\frac{\Delta_{0,xy^+}}{2\hbar}\sum_{x}\left(C_{xy^+} - C^*_{xy^+}\right), \quad (3.6)$$

$$\frac{dC_{xy^+}}{dt} = i\frac{\Delta_{0,xy^+}}{2\hbar}\left(n_{I,y^+} - n_{A,x}\right) - \frac{C_{xy^+}}{T_{2xy^+}} - i\frac{E_{xy^+}}{\hbar}C_{xy^+}, \quad (3.7)$$

$$\frac{dC_{y^-x}}{dt} = i\frac{\Delta_{0,y^-x}}{2\hbar}\left(n_{A,x} - n_{I,y^-}\right) - \frac{C_{y^-x}}{T_{2y^-x}} - i\frac{E_{y^-x}}{\hbar}C_{y^-x}, \quad (3.8)$$

In Eqs. (3.4)–(3.8), n is the carrier density in the levels of the active and injector regions. Subscripts A and I denote active and injector regions, respectively. Indices x and y indicate the levels in the active and injector regions, respectively. Superscripts $-$ and $+$ indicate the subband for which density equation is written in the injector region that precedes and follows the active region, respectively. The quantity C_{xy} denotes the coherence between levels x and y. The parameter s_{xy} denotes the scattering time between levels x and y. The parameter $\Delta_{0,xy}$ denotes the energy splitting at resonance between levels x and y involved in tunneling, while E_{xy} is the detuning of the energy of level x (E_x) and the energy of level y (E_y) from resonance. The parameter $T_{2,xy}$ is the coherence time between levels x and y.

3.3.1 Scattering Time s_{xy}

Electron-LO phonon intersubband scattering is the dominant intersubband scattering mechanism for mid-IR QCLs [33, 34]. However, electron-electron scattering plays significant role when LO phonon transitions are forbidden with subband energies sufficiently close to one-another [35, 36]. Thus, the scattering rate between subband $|x\rangle$ and $|y\rangle$ is

$$\frac{1}{s_{xy}} = \frac{1}{s_{xy}^{\mathrm{e-LO}}} + \frac{1}{s_{xy}^{\mathrm{e-e}}} \tag{3.9}$$

where $s_{xy}^{\mathrm{e-LO}}$ and $s_{xy}^{\mathrm{e-e}}$ are the scattering lifetimes of an electron between levels $|x\rangle$ and $|y\rangle$ due to electron-LO phonon and electron-electron scattering, respectively. To calculate electron-LO phonon interaction, both absorption and emission phenomena have been taken into account by

$$\frac{1}{s_{xy}^{\mathrm{e-LO}}} = \frac{1}{s_{x\to y}^{\mathrm{e-LO,emission}}} + +\frac{1}{s_{x\to y}^{\mathrm{e-LO,absorption}}} \tag{3.10}$$

3.3.2 Coherence Time $T_{2,xy}$

The coherence between any two levels x and y decays in a time $T_{2,xy}$, as the propagating electronic wave-packets lose phase coherence mainly due to intrasubband scattering [37]. The scattering mechanisms that dominate the coherence decay are electron-electron scattering, electron-LO phonon scattering, and electron-interface roughness scattering [38, 39]. So, the coherence time $T_{2,xy}$ between levels x and y can be written as [29]

$$\frac{1}{T_{2,xy}} = \frac{1}{T_{2,xy}^{\mathrm{e-LO}}} + \frac{1}{T_{2,xy}^{\mathrm{e-e}}} + \frac{1}{T_{2,xy}^{\mathrm{e-Roughness}}} \tag{3.11}$$

where $T_{2,xy}^{\mathrm{e-LO}}$, $T_{2,xy}^{\mathrm{e-e}}$ and $T_{2,xy}^{\mathrm{e-Roughness}}$ are the contributions to the coherence time by scattering due to electrons, LO phonons, and interface roughness, respectively.

The scattering of an electron in subband $|x\rangle$ due to an electron or an LO phonon is

uncorrelated with the scattering of an electron in subband $|y\rangle$ due to an electron or an LO phonon [40, 41]. Therefore, intrasubband electron-electron and electron-LO phonon transitions in levels x and y separately contribute to the loss of phase coherence and the rates add linearly [23]. In our model, we consider the dominant intrasubband electron-electron transitions, i.e., $x, x \rightarrow x, x$ and $y, y \rightarrow y, y$, and we neglect the less significant intrasubband electron-electron scattering, such as $x, y \rightarrow x, y$. Thus,

$$\frac{1}{T_{2,xy}^{e-e}} = \frac{1}{s_{x,x\rightarrow x,x}^{e-e}} + \frac{1}{s_{y,y\rightarrow y,y}^{e-e}}, \tag{3.12}$$

where $s_{x,x\rightarrow x,x}^{e-e}$ is the scattering lifetime due to $x, x \rightarrow x, x$ electron-electron transitions.

3.4 Carrier Transport with NIR Injection

When NIR light is coupled into the QCL cavity, electron-hole pairs are created with electrons photo-excited to the conduction band. The amount of photo-excited carriers to the conduction band depends on the intensity and wavelength of the NIR light, and the design and material used in the QCL. The photo-excited carriers can significantly populate a conduction band state if the NIR light has a wavelength which is in resonance with the separation between valence and conduction band states. Therefore, the density matrix formulation for the conduction band states given in Eqs. (3.4)–(3.8) will have additional electron scattering rates due to interband electron transition. We can write the

density equations for one and half periods of the QCL structure as

$$\frac{dn_{A,x}}{dt} = \sum_{x'\neq x}\frac{n_{A,x}}{s_{x'x}} + \sum_{y^-}\frac{n_{I,y^-}}{s_{y^-x}} + \sum_{y^+}\frac{n_{A,y^+}}{s_{y^+x}} - \sum_{y^-}\frac{n_{A,x}}{s_{xy^-}} - \sum_{x'\neq x}\frac{n_{A,x}}{s_{xx'}} - \sum_{y^+}\frac{n_{A,x}}{s_{xy^+}}$$
$$- i\frac{\Delta_{0,xy^+}}{2\hbar}\sum_{y^+}\left(C_{xy^+} - C^*_{xy^+}\right) + i\frac{\Delta_{0,y^-x}}{2\hbar}\sum_{y^+}\left(C_{y^-x} - C^*_{y^-x}\right) + \sum_{j'=1}^{N_v} r(f_{A,x}, f_{v,j'}), \quad (3.13)$$

$$\frac{dn_{I,y^-}}{dt} = \sum_{y^{-\prime}\neq y^-}\frac{n_{I,y^{-\prime}}}{s_{y^{-\prime}y^-}} + \sum_{x}\frac{n_{A,x}}{s_{xy^+}} + \sum_{x}\frac{n_{A,x}}{s_{xy^-}} - \sum_{x}\frac{n_{I,y^-}}{s_{y^-x}} - \sum_{x}\frac{n_{I,y^+}}{s_{y^+x}} - \sum_{y^{-\prime}\neq y^-}\frac{n_{I,y^-}}{s_{y^-y^{-\prime}}}$$
$$- i\frac{\Delta_{0,y^-x}}{2\hbar}\sum_{x}\left(C_{y^-x} - C^*_{y^-x}\right) + i\frac{\Delta_{0,xy^+}}{2\hbar}\sum_{y^+}\left(C_{xy^+} - C^*_{xy^+}\right) + \sum_{j'=1}^{N_v} r(f_{I,y^-}, f_{v,j'}), \quad (3.14)$$

$$\frac{dn_{I,y^+}}{dt} = \sum_{y^{+\prime}\neq y^+}\frac{n_{I,y^{+\prime}}}{s_{y^{+\prime}y^+}} + \sum_{x}\frac{n_{A,x}}{s_{xy^+}} + \sum_{x}\frac{n_{A,x}}{s_{xy^-}} - \sum_{x}\frac{n_{I,y^-}}{s_{y^-x}} - \sum_{x}\frac{n_{I,y^+}}{s_{y^+x}} - \sum_{y^{+\prime}\neq y^+}\frac{n_{I,y^+}}{s_{y^+y^{+\prime}}}$$
$$- i\frac{\Delta_{0,y^-x}}{2\hbar}\sum_{x}\left(C_{y^-x} - C^*_{y^-x}\right) + i\frac{\Delta_{0,xy^+}}{2\hbar}\sum_{x}\left(C_{xy^+} - C^*_{xy^+}\right) + \sum_{j'=1}^{N_v} r(f_{I,y^+}, f_{v,j'}), \quad (3.15)$$

$$\frac{dC_{xy^+}}{dt} = i\frac{\Delta_{0,xy^+}}{2\hbar}\left(n_{I,y^+} - n_{A,x}\right) - \frac{C_{xy^+}}{T_{2xy^+}} - i\frac{E_{xy^+}}{\hbar}C_{xy^+}, \quad (3.16)$$

$$\frac{dC_{y^-x}}{dt} = i\frac{\Delta_{0,y^-x}}{2\hbar}\left(n_{A,x} - n_{I,y^-}\right) - \frac{C_{y^-x}}{T_{2y^-x}} - i\frac{E_{y^-x}}{\hbar}C_{y^-x}. \quad (3.17)$$

Here, $f_{v,j'}$ and $f_{c,x}$ are valence and conduction subband fermi-dirac distribution functions and $r(f_{c,x}, f_{v,j'})$ is the carrier transition rate from valence band to conduction band.

3.4.1 Calculation of $r(f_{A,x}, f_{v,j'})$

We have discussed the calculation of interband absorption coefficient in Sec. 2.3. The absorption coefficient is a direct function of the density of states of valence band and conduction band, and also the overlap and energy difference between conduction and valence subband in consideration, as shown in Eq. (2.31).

The absorption coefficient is a measure of the portion of absorbed light flux when a light pulse is propagated through the structure. The number of excited electron-hole pair

generation is equal to the number of net interband transitions. Thus, change in carrier dn_P per unit time per unit area can be calculated as

$$dn_P = d\phi = \alpha\phi dz\,, \tag{3.18}$$

where α is interband absorption coefficient and ϕ is the light flux. The total carrier generated per unit area per unit time is calculated by integrating Eq. (3.18) over the length of the structure l

$$n_P = \int_0^l d\phi = \int_0^l \alpha\phi dz. = \alpha\phi l\,. \tag{3.19}$$

Now, the light flux ϕ is defined as the number of photons per second per unit area i.e., ϕ = No. of Photons/ Area $\times$ Time. Thus, it can be expressed as

$$\phi = \frac{P}{Ah\nu}\,, \tag{3.20}$$

where, P is the coupled optical power. P depends on the physical coupling of the injected NIR light into the cavity. Typical values for external light coupling for QCL cavities are ~10–15% [42].

Thus, the number of carriers generated per unit time per unit area is

$$n_P(\omega) = \frac{P\alpha(\omega)l}{Ah\nu}\,. \tag{3.21}$$

Now, if the NIR had a single frequency ω, photo-excitation would have been if only there were a resonance of $\hbar\omega$ between valence and conduction band states. However, practically, light pulses are usually of a finite linewidth. If we consider a Lorentzian light pulse, carrier generation at a frequency ω will depend on the amount of overlap between the light pulse and the absorption spectrum. Considering the correlation between the light

pulse and the absorption spectra, the carrier generation rate becomes:

$$n_P(\omega) \;=\; \frac{P\alpha(\omega)l}{Ahv} \times c(\omega)\;, \tag{3.22}$$

where $c(\omega)$ is the overlapping factor, and can be calculated as $c(\omega) = L(\omega)\alpha(\omega)/$ Maximum of $L(\omega)$. Here, $L(\omega)$ is the frequency domain representation of the NIR pulse.

Now, the carrier generation rate per unit area due to photoexcitation from valence subband to conduction subband $|x\rangle$ can be written as

$$r = n_P(hv_x) \times L(t)\;, \tag{3.23}$$

where $L(t)$ is the time domain representation the light pulse. The NIR pulse can be a square pulse train with a temporal pulsewidth in pico-second or femto-second range and repetition rate in KHz range. For example, for a square pulse introduced into the rate equations at time $t = t_0$ with temporal pulse width of t_w, the carrier transition rate will be

$$r = \frac{P\alpha l}{Ahv}[u(t - t_0) - u(t - t_0 - t_w)]. \tag{3.24}$$

Thus, this rate will start contributing to the subband population scattering rate calculations at $t = t_0$ and stop at $t = t_0 + t_w$.

Usually, the carrier density is expressed in per unit volume, and thus, Eq. (3.21) is divided by the L. For time dt, the number generated carrier per unit volume will equal to:

$$n_P \;=\; \frac{\alpha P}{Ahv}\int_0^t \mathrm{d}t, \tag{3.25}$$

The maximum of carriers will be generated when the time pulse duration will exceed

spontaneous lifetime, and thus

$$n_{P_{max}} = \frac{\alpha P \tau_{sp}}{Ah\nu} . \tag{3.26}$$

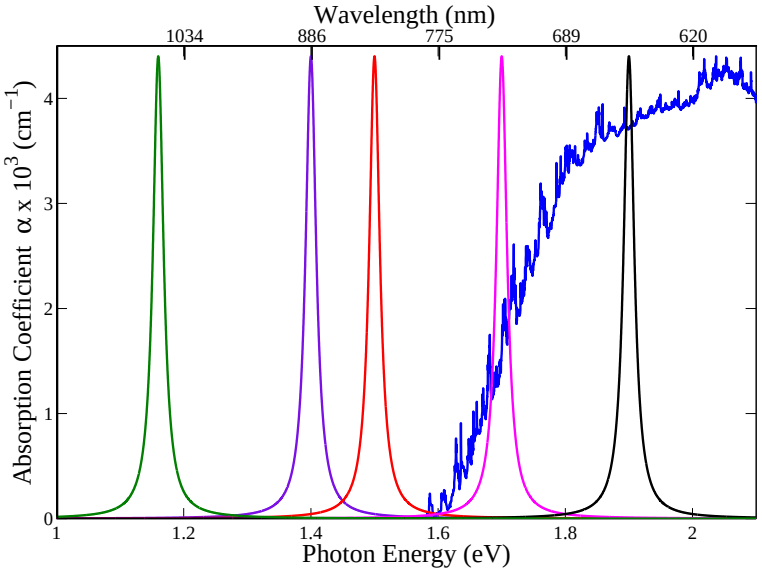

Figure 3.2: Interband absorption spectrum for the QCL structure in Ref. [42]. Lorentzian NIR pulses of different wavelengths are also plotted to show the overlap with the absorption spectrum

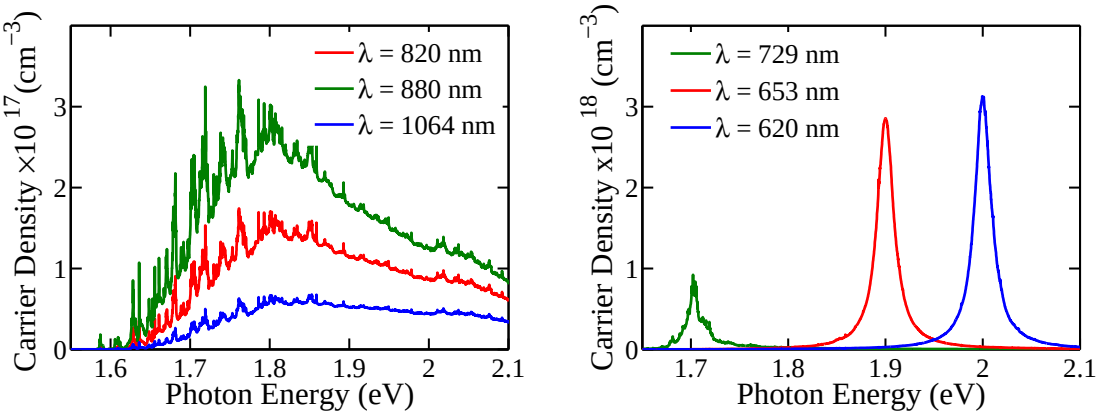

Figure 3.3: Calculated maximum excited carrier densities for the absorption spectrum shown in Fig. 3.2 and different NIR to visible wavelengths.

Now, we plot the interband absorption spectrum for the QCL structure described in Ref. [42] operated at 60 kV/cm bias electric field and injected with NIR pulses of wave-

length 1064 nm (Ti:Sapphire laser), 880 nm, 820 nm (Laser diodes), 720 nm and 650 nm in Fig. 3.2. Ideally, the light contains infinite frequencies as we considered a square time-domain pulse. Typically, we use a Lorentzian light pulse with finite linewidth of 10 meV as the excitation pulse. We calculated the maximum generated carriers using Eq. (3.26), the result of which are plotted in Fig. 3.3. As we see from Fig. 3.2 and Fig. 3.3, when the overlap of the excitation NIR or visible pulse with the absorption spectrum increases, the carrier density increases. One interesting thing that we notice is that, there are considerable carrier densities even when the NIR pulse has a center wavelength of 886 nm (1.40 eV), which is less than the bandgap of the QCL. The reason behind is the broadening of NIR pulse, which results in the overlap of the absorption spectra and light pulse tail. We also note from Fig. 3.3 that for higher energy NIR pulses, carriers are distributed more in the high energy region. Thus, with high energy pulses, more hot carriers are generated due to the high-k tail of the electron distribution.

3.5 Poisson Potential due to Photo-excited Carriers

In a system where a large number of charge carriers are present, they can give rise to a significant additional potential on top of the usual band-edge potential. The additional potential $V_\rho(z)$ arising from a charge distribution ρ, can be expressed using Poisson's equation

$$\nabla^2 V_\rho = -\frac{\rho}{\epsilon}, \tag{3.27}$$

where ϵ is the permittivity of the material. The solution to Eq. (3.27)

$$V_\rho(\mathrm{r}) = \int_{-\infty}^{\mathrm{r}} \mathrm{E} \,.\, d\mathrm{r}, \tag{3.28}$$

where $\mathrm{E} = -\nabla V$.

If $D(z)$ is the volume density of the dopants at position z, then the total number of carriers,

per unit cross-sectional area, is given by

$$N \;=\; \int_{-\infty}^{\infty} D(z)\mathrm{d}z \tag{3.29}$$

The net charge density distributed over n number of subbands is

$$\sigma(z) \;=\; q\left(\sum_{i=1}^{n} N_i\psi_i^*(z)\psi_i(z) \;-\; D(z)\right)\delta z \tag{3.30}$$

where, $\sum_{i=1}^{n} N_i \;=\; N$.

When a mid-IR QCL is pumped by a NIR laser, carriers are excited from valence subbands to conduction subbands as discussed in Sec. 3.4. Thus electron density in the conduction band is increased as well as holes are created in the valence subbands. From Sec. 3.4.1, we note that the number of generated electron-hole pair is quite large, thus their contribution to band bending is not negligible.

Let us assume that, after electrons are photo-excited from the valence band, the electron density per unit area in conduction subband $|i\rangle$ is $N'_{c,i}$ and the hole density per unit area in valence subband $|j\rangle$ is $N'_{v,j}$. Then from charge-neutrality, we can calculate the sheet charge density similar to Eq. (3.30)

$$\sigma(z) \;=\; q\left(\sum_{i=1}^{n_c} N'_{c,i}\psi^*_{c,i}(z)\psi_{c,i}(z) \;-\; \sum_{j=1}^{n_v} N'_{v,j}\psi^*_{v,j}(z)\psi_{v,j}(z) \;-\; D(z)\right)\delta z. \tag{3.31}$$

To simplify things, we recall that, the doping density in a QCL structure is considerably low (typically $10^{17}\mathrm{cm}^{-3}$ in GaAs/AlGaAs system [42]) and usually done only in injector region to avoid effect of space charge localization. Thus, we can neglect the contribution from doping in Eq. (3.31) and write

$$\sigma(z) \;=\; q\left(\sum_{i=1}^{n_c} N^{\text{excited}}_{c,i}\psi^*_{c,i}(z)\psi_{c,i}(z) \;-\; \sum_{j=1}^{n_v} N^{excited}_{v,j}\psi^*_{v,j}(z)\psi_{v,j}(z)\right)\delta z, \tag{3.32}$$

where $N_{c,i}^{\text{excited}}$ and $N_{v,j}^{\text{excited}}\psi_{v,j}$ are excited carrier distribution in the conduction and valence subbands respectively, due to external light injection.

Then, we can find the solution to Eq. (3.27) to find V_ρ using Eq. (3.28). Now, the new band-edge potential will be:

$$V'_{CB} \;=\; V_{CB} \;+\; V_\rho \tag{3.33}$$

Let us apply Eq.(3.32) to the quantum cascade laser structure described in [42]. The QCL structure is optically pumped using a 1.50 eV (0.82 μm) NIR source, for which we have already discussed the electron-hole pair generation rate in Sec.3.4.1. From Fig. 3.3, we find that, the amount of excited electron-hole pairs is comparable to that of the QCL own carrier concentration from doping ($n = 2 \times 10^{17}$ cm^{-3}). Thus, we calculate the areal charge density σ due to the excited electron and holes using Eq. (3.32) and resultant electric field E and the additional potential $V_\rho(z)$ using Eq. (3.28). The results are presented in Fig. 3.4, where it is evident from the charge density plot that it maintains charge neutrality. Here, we have taken $1\frac{1}{2}$ period of the structure i.e., an injector region, an active region and a collector region (so called I-A-I structure) to incorporate the effect of periodicity into Poisson potential.

Ideally, the contribution from the excited carriers should be added to the potential profiles of both conduction and valence bands. Thus, the potential term in multi-band $\vec{k}\cdot\tilde{\mathbf{p}}$ method hamiltonian described in Eq. (2.6) should account for total band edge potential considering V_ρ. However, we can neglect the effect of Poisson potential on valence band under the assumption that the band-bending of the valence band does not change the interband absorption spectrum considerably. As we have seen, the interband absorption spectrum is not merely the summation of the delta functions corresponding to the valence band to conduction band transitions, rather it is broadened due to the contribution of high-k electrons. Thus, extra Poisson potential on the valence band edge will not disrupt the interband absorption spectrum considerably. Again, QCL being a unipolar intersub-

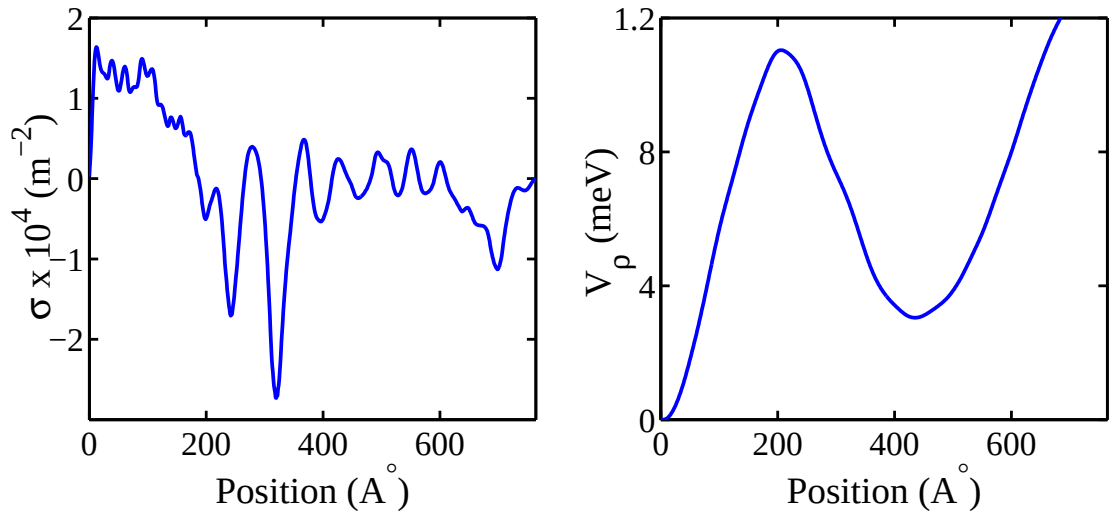

Figure 3.4: (a) Areal charge density σ for the QCL structure after 4 *ps* NIR (.82 μm) pulse injection (b) Resultant Poisson's potential V_ρ due to the excited carrier density in (a)

band laser, literatures like Refs. [3, 5] have used single band effective-mass Schrodinger equation to calculate the electronic states in play neglecting the coupling from valence band. Hence, to reduce the calculation burden, we assume the pronounced effect of photoexcited carriers is on conduction band bending, and thus design the self-consistent Schrodinger-Poisson solver considering only single band effective mass equation.

We followed the iterative approach to solve the electronic states self-consistently [20], i.e., after solving Schrodinger equation, calculating the potential due to the charge distribution, we add it to the original band-edge potential, then solve Schrödinger's equation again, and so on. The process is illustrated in Fig. 3.5.

3.6 Change of Refractive Index

When a QCL is illuminated by a NIR pulse at its front facet, the NIR pulse intensity varies within the cavity. However, to simplify modeling, we assume an average constant

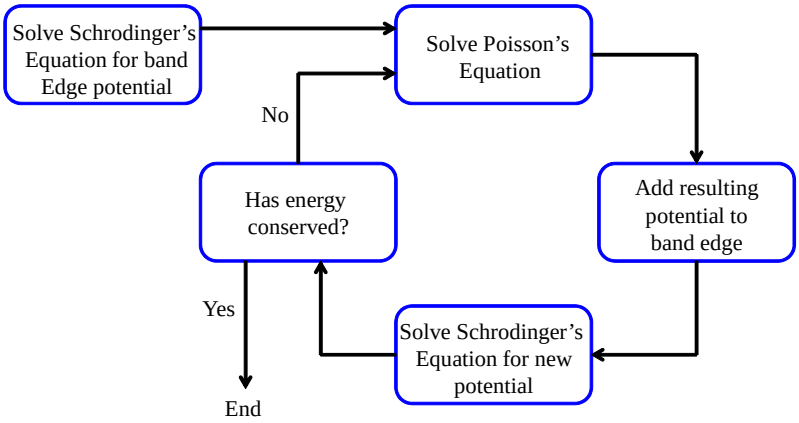

Figure 3.5: Block diagram illustrating the process of self-consistent iteration

intensity throughout the cavity. In Sec. 3.4.1, we discussed the excited carrier density considering a constant optical power throughout the cavity. These extra carriers are likely to change the effective refractive index of the active region and cladding region, where they are generated.

We assumed that the major contribution to the change in the structure conductivity is given by the electrons since the transport of holes in the growth direction is almost completely blocked by the barriers. The contribution of photo excited carriers to the effective refractive index can be estimated using Drude model as [11]

$$\Delta n_{eff} \approx -n_0 \left(\Gamma_c \frac{\omega_{pc}^2}{2\omega^2} + \Gamma_a \frac{\omega_{pa}^2}{2\omega^2} \right), \tag{3.34}$$

where $\omega_{pc,pa}^2 = \frac{\Delta N_{c,a} e^2}{\epsilon_0 m_e^{*2}}$ and $N_{c,a}$ is the excited carrier density due to optical pulse injection. We can neglect the cladding layer contribution in Eq. (3.34) as the confinement factor Γ_c is very small (typical values are around 0.17). For the active region, we take a typical value for the confinement factor Γ_a of 0.53. Equation (3.34) is valid only for $\omega_p << \omega$.

The decrease in refractive index shifts the sustainable modes in the cavity to higher energy values. However, the change is very small to play any significant part in shifting the emission wavelength.

3.7 Summary

In this chapter, we have provided a detailed analysis of the effect of NIR injection on QCL gain. We introduced the modified carrier transport model with photoexcited carriers, which includes the dominant scattering mechanism in a QCL structure. The effect of photoexcited carriers on band bending is modelled. Also, the change of refractive index, and its effects on the emission modes due to photoexcited carriers are also discussede. Thus, this chapter provides a comprehensive modeling of gain when a mid-IR QCL is optically pumped using a NIR pulse.

Chapter 4

Gain and Wavelength Modulation of QCL with Optical Pumping

4.1 Introduction

All optical modulation (OOM) of QCL exploits QCL's intrinsic ultra-fast carrier recovery time and enable us to overcome bandwidth limitation arising from parasitic effects of electrical circuitry. First, demonstration of OOM was reported by Zervos et al. [8], who observed reduction of QCL threshold with injection of NIR. However, this finding has directly been contradicted by the experimental observations of Sekine et al. [9], Chen et al. [6, 10] and Suchalkin et al. [11]; where they reported the increase of threshold current and thereby decrease of QCL output intensity with external NIR injection. Suchalkin et al. and Yang et al. [11, 12, 15, 16] also reported wavelength modulation of mid-IR QCL due to NIR injection, which they attributed to the change in effective refractive index due to the extra carrier generated in the active region and cladding layer.

In the previous chapter, we have discussed the modeling of NIR injection effects on mid-IR QCL. In this chapter, we will briefly introduce the simulation flow and then present our results which is in excellent agreement with the experimental results. The NIR wave-

length dependence of intersubband gain of QCL can explain the contradiction between the experimental observations. The results also shows a frequency modulation which can be controlled by changing the NIR power.

4.2 Gain Modulation with Photo-Excitation

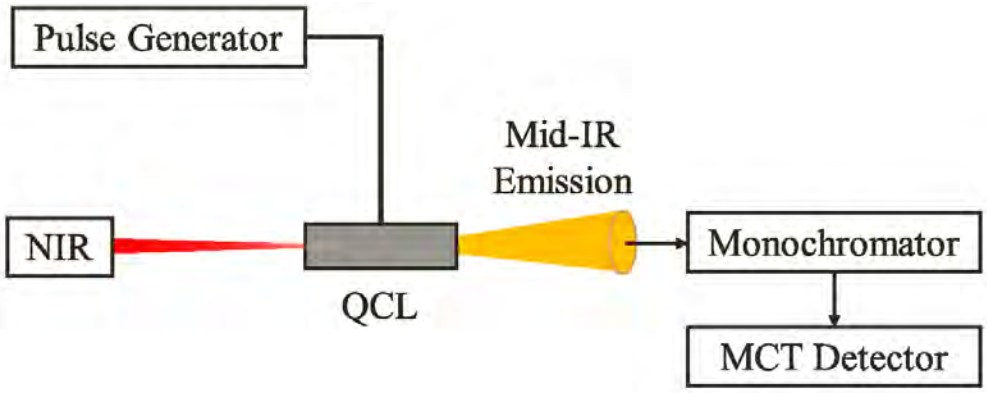

Figure 4.1: Schematic of the experimental setup for gain and frequency modulation of a QCL by injecting NIR light.

We have presented a schematic view of the experimental set-up in Fig. 4.1. We assume that a ultra-short square NIR pulse is used to optically pump the QCL. The NIR pulse excites carriers from valence band to conduction band, thereby creating electron-hole pairs. Only those transition energies supported by the NIR pulse will be allowed and the respective conduction subbands' electron densities will be increased. Simultaneously, holes will be created in valence subbands. We have illustrated the interband transitions for different NIR wavelengths in a schematic in Fig. 4.2. Here, the red arrow signifies NIR pusle energy of 1.4 eV which is 30 meV less than the QCL bandgap of 1.43 eV.

The spatial distribution of the photoexcited carriers in both conduction and valence bands will give rise to a Poisson potential as discussed in Sec. 3.5. However, the electron mobility is almost thrice of hole mobility in GaAs, thus we can neglect the spatial- and temporal-redistribution of holes in the valence band. Finally, we will calculate the time

dependent carrier densities in a typical QCL structure using the formalism developed in Sec. 3.4 and with the steady state population densities, we will calculate the intersubband gain.

4.3 GaAs/AlGaAs QCL Structure

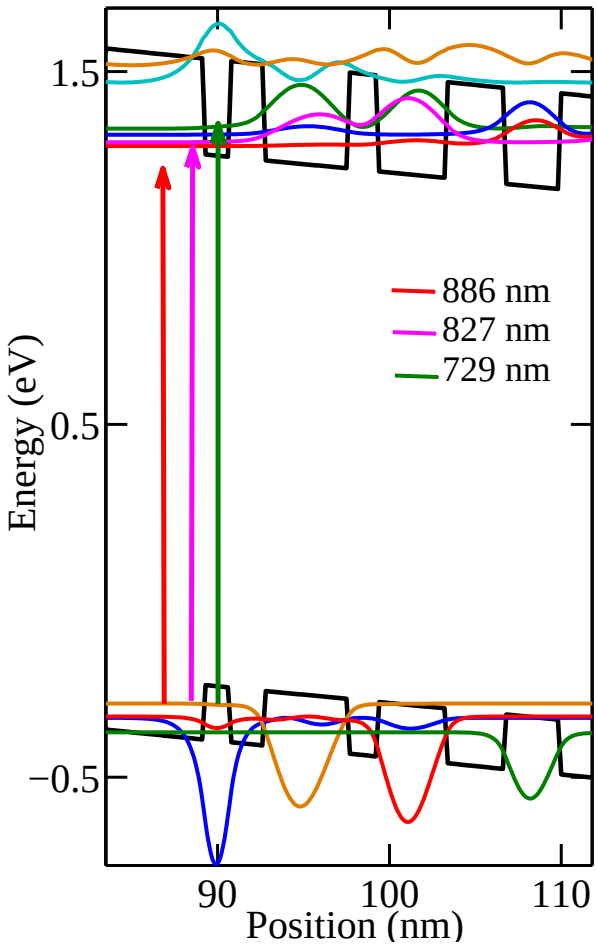

Figure 4.2: Conduction and valence band structures and moduli-squared wavefunctions at 41 kV/cm. Arrows showing carrier transition from valence to conduction band to create ehp for different NIR wavelengths.

We consider the QCL structure described in Ref. [42] for three bias electric fields to study three distinct cases: (a) Just below threshold when the lasing gain is less than cavity losses, (b) at a moderate electric field above threshold, and (c) at the highest electric

field value that the laser operates with. In each case, we optically pump the laser with NIR square pulses with pulse width of 4 ps when the QCLs are operating at steady-state. We study the change in gain due to the introduction of the NIR light with the gain medium. We vary the wavelength of the NIR to 729 nm, 827 nm, and 886 nm since these wavelengths range from being very close to GaAs bandgap (886 nm) to 300 meV over the band-gap, thus essentially covering the significant part of the interband absorption spectrum of the QCL.

4.3.1 Laser Operating Below Threshold

At 41 kV/cm bias electric field, the laser gain is not sufficient to support the cavity losses. The band structure in Fig. 4.3(a) shows that the injector ground, i.e., level 8 is not sufficiently aligned with the active region upper lasing level, i.e., level 9 to produce significant carrier inversion between the upper and lower lasing levels (level 9 and 6, respectively). In Fig. 4.3(b). we show the calculated gain spectrum of this QCL. We note that, even the peak gain is much smaller than typical cavity losses in QCL, which is ~10–15 cm^{-1} [42]. Therefore, this QCL cannot produce a sustained oscillation of radiation at 41 kV/cm.

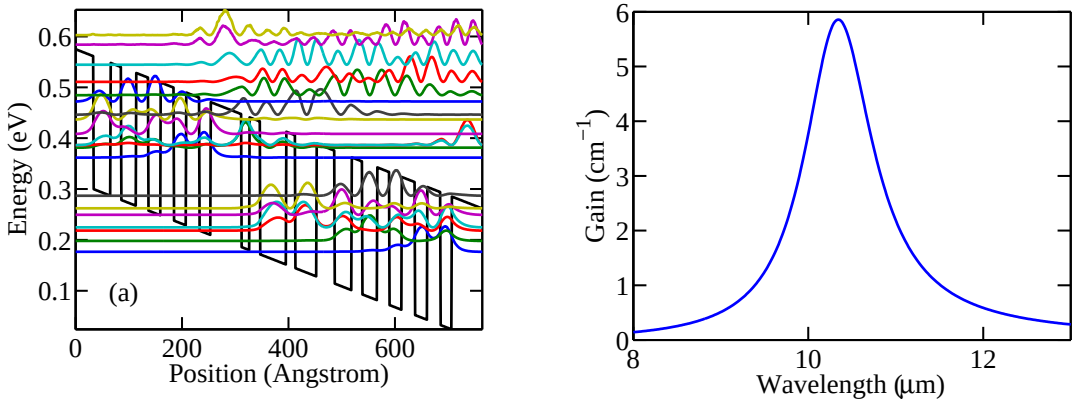

Figure 4.3: (a) Band structure and moduli-squared wavefunctions at 41 kV/cm (b) Gain spectrum at 41 kV/cm.

4.3.1.1 Excitation by 886 nm NIR Pulse

Let us assume, we inject the laser with a NIR pulse of 10 mW power and wavelength 886 nm, which is almost equal to GaAs bandgap of 1.43 eV. Extra electron-hole pairs will be generated which change the band structure significantly and decrease the effective refractive index, which in effect shifts the modes to higher photon energy. Due to the photoexcited carriers, carrier densities at different subbands increase.

We plot the electronic band structure with band bending in Fig. 4.4(a) and the time dependent carrier densities at different subbands in Fig. 4.4(b). We note that, the new lower lasing level is now level 5 and new upper lasing level is level 10 and and we see a significant increase in carrier density in injector ground, i.e., level 8 and also upper laser level, i.e., level 10. There is a significant increase in population inversion between the new two lasing levels as depicted by the red double arrow in Fig. 4.4(b). The reason behind this significant increase in population inversion can be attributed to the proper alignment of the injector ground with the active region upper lasing level, which ensures resonant tunneling of carriers. The dipole element between the new lasing level pairs increases which indicate more overlap between these two levels. The dipole element and population inversion both increase after optical pulse injection as indicated in Table. 4.1; thus, peak gain is expected to increase.

The emission wavelength depends on the energy difference between the two-lasing levels. As the upper lasing level shift to a higher energy state, the emission wavelength is expected to shift to a higher wavenumber. The new energy difference between the two lasing levels ($E_{5\rightarrow11}$ = 126 meV) is larger than the unexcited case. The excited carriers also decrease the effective refractive index of the cavity, thus the modes shift to higher photon energy. So, the lasing wavelength is expected to shift to higher wavelength values.

In Fig. 4.5 we have plotted the gain spectrum after photo-excitation for 2 different

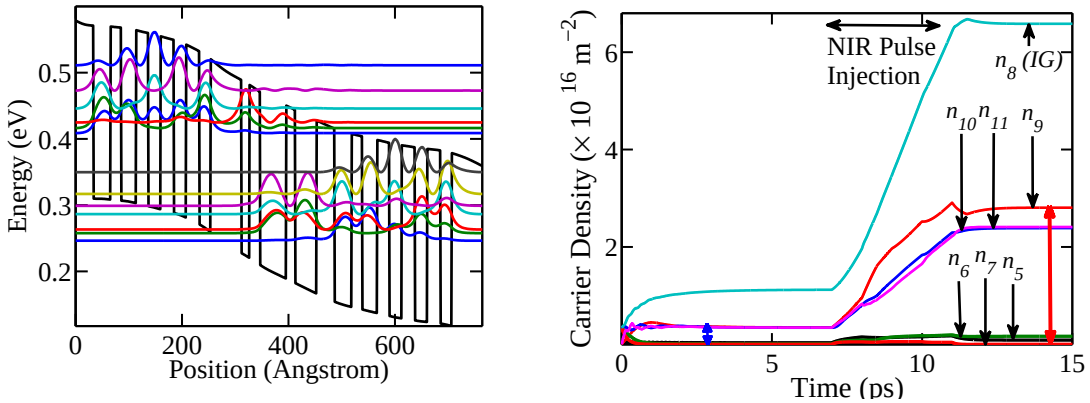

Figure 4.4: (a) Band structure and moduli-squared wavefunctions at 41 kV/cm with excited carrier band bending for NIR pulse output power of 10 mW, coupling 10%(b) Carrier distribution for the condition in (a)

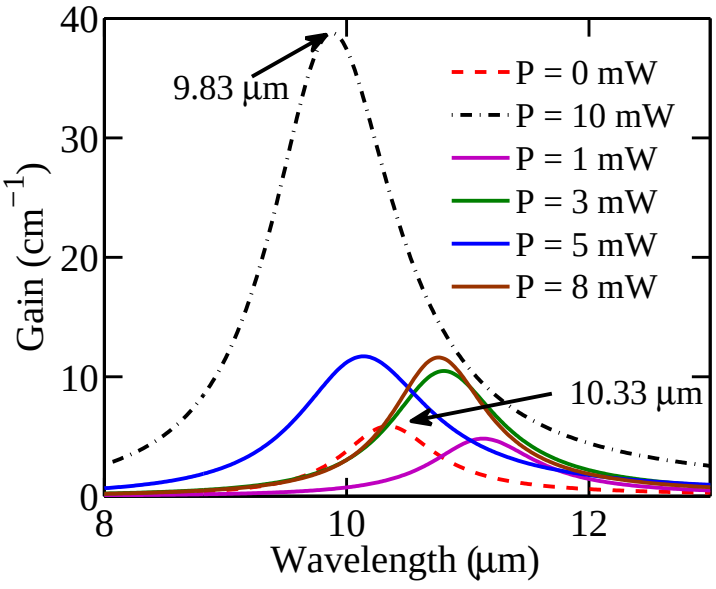

Figure 4.5: Gain spectrum for the structure in [42] after photo-excitation using a NIR pulse of 0.886 μm for 4 ps. Here P denotes the IR pulse average power. The emission wavelength shows a blue-shift with NIR pulse power increase.

NIR optical power. As we can see from the figure, when the NIR optical power is 10 mW, the gain sufficiently increases as expected. Lasing action will happen just below threshold, as the gain after NIR pumping overcomes the cavity losses. This was experimentally demonstrated by Zervos et al. [8]. The output emission wavelength of the QCL also shows a blue shift with increase of NIR power. The dominant mechanism here is the shift of upper lasing level to higher energy values. The mode frequency shift to higher photon values due to refractive index change plays a less dominant role.

Table 4.1: Dipole Element and Population Inversion Comparison (Before and After Injection)

	Before Excitation		After Excitation	
	ULL = 9	LLL = 6	ULL = 10	LLL = 5
Population Inversion ($\times 10^{14}$)	3.15		22.2	
Dipole Moment ($\times 10^{-9}$)	1.3		1.48	
Dipole Moment ($\times 10^{-9}$) between IG and ULL	3.8		6.6	

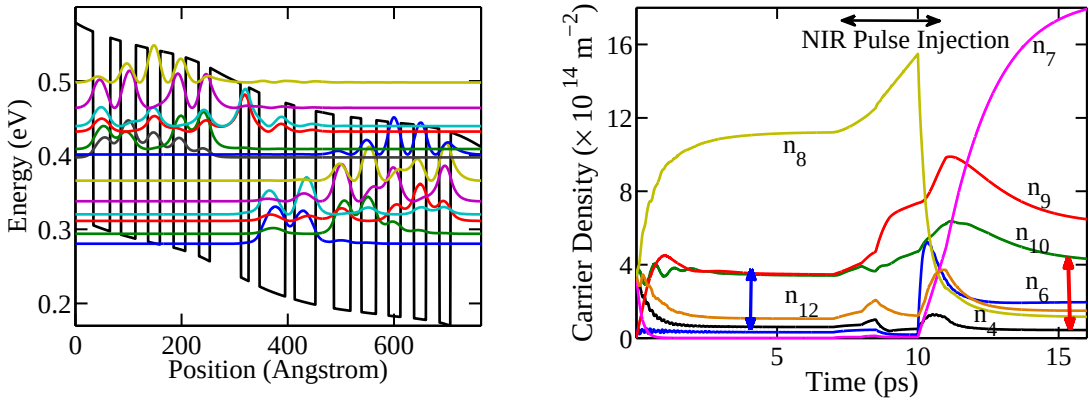

Figure 4.6: (a) Band structure and moduli-squared wavefunctions at 41 kV/cm with excited carrier band bending for NIR pulse output power of 1 mW. (b) Carrier distribution for the condition in (a). Carrier distribution is shown for only the optically important electronic states.

However, we notice from Fig. 4.5, a slight decrease of mid-IR QCL gain when the NIR pulse power is reduced by a factor of 10. The electronic states and carrier distribution are plotted for this case in Fig. 4.6. We find that the alignment between the upper lasing

level and injector ground, i.e., levels 10 and 9, respectively, is not increased sufficiently to change the population inversion for this pumping power. Hence, we find that the population inversion value does not increase even after excited carrier injection in Fig. 4.6(b).

4.3.1.2 Excitation by 827 nm NIR Pulse

Let us assume, we excite the QCL with a 827 nm Ti:Sapphire laser pulse with pulse-width 4 ps. In Fig. 4.7, we have plotted the gain spectrum for 827 nm NIR pulse injection

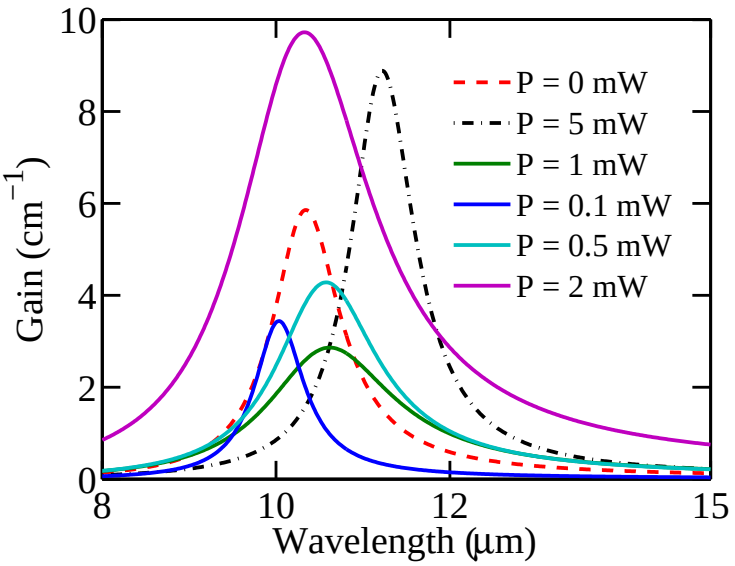

Figure 4.7: Gain spectrum for the structure in [42] after photo-excitation using a NIR pulse of 0.827 μm for 4 ps.

for different injection powers. We notice similar changes in gain for this NIR wavelength to the 886 nm pulse. Gain increases when NIR pump power is 5 mW, but it decreases slightly when the pump power is 10 times smaller.

4.3.1.3 Excitation by 729 nm NIR Pulse

Here, we consider a case where the QCL is injected with a NIR pulse of 729 nm with pump power of 10 mW. The NIR pulse energy is significantly greater than the bandgap, thus, hot carriers are generated due to photo-excitation. Carrier densities at the subbands are increased and additinal band-bending is introduced. We have plotted the band struc-

ture in Fig. 4.8(a) and corresponding carrier densities in the subbands in Fig. 4.8(b). From Fig. 4.8(a), we see that the ULL is level 12 and LLL is level 1. The population inversion between these two levels is significantly smaller as shown by the red double arrow in Fig. 4.8(b). To understand the carrier transport, we note from Fig. 4.8(b) that at steady state, a large number of photo excited electrons accumulate in levels 5 and 7, which are spatially localized away from the active quantum wells as marked by the red circle in the band structure of Fig. 4.8(a). These levels, though being injector levels, can not contribute to ULL population as they are energetically and spatially distant from the ULL. Also, the dipole moment between the two new lasing levels is significantly reduced. Thus, peak gain will decrease. We have plotted the intersubband gain for two

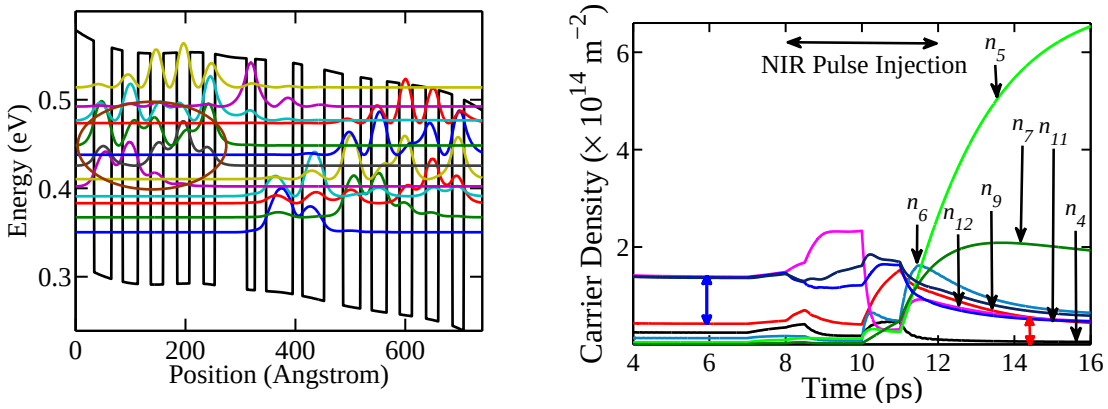

Figure 4.8: (a) Band structure and moduli-squared wavefunctions after optical pumping with pump power 1mW. (b) Band structure and moduli-squared wavefunctions after optical pumping with pump power 1mW. (b)

different NIR powers in Fig. 4.9. In both of the cases, the gain is decreased significantly as expected.

Now, if we want to compare between the two contradictory phenomena described in Sec. 4.3.1.3 and Sec. 4.3.1.1, we should look into the initial excited carrier distribution over space and energy plotted in Fig. 4.10. When the NIR wavelength is near the QCL band-gap energy, more carriers are accumulated in the injector ground. It contributes to increased population of the ULL as shown in Fig. 4.4 through resonant tunnelling.

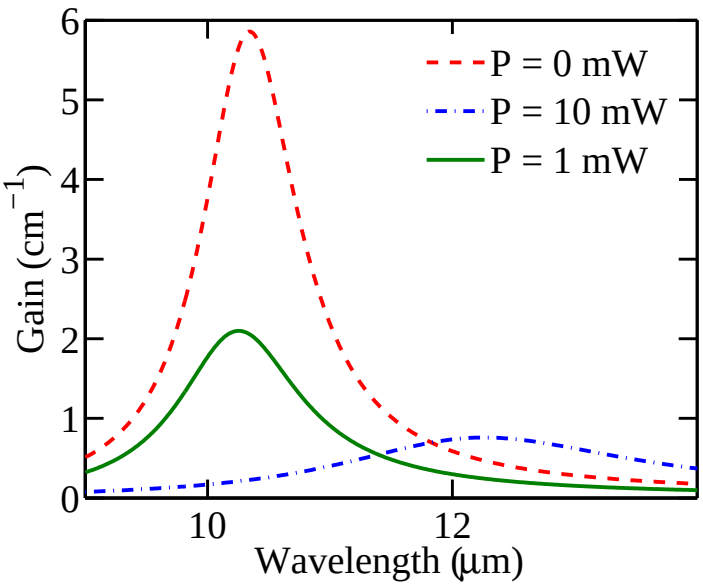

Figure 4.9: (a) Gain spectrum at 41 kV/cm after 729 nm pulse injection for 4 ps. In every cases, gain decreases and lasing does not occur below threshold

In this case, the band bending potential acts to aid the alignment between ULL and IG. But, for a NIR pulse of energy much greater than bandgap, hot electrons accumulate near upper injector levels. These electrons emit LO-phonons and finally accumulate in the lower injector levels as shown in Fig. 4.8. The band-bending potential disrupts the proper carrier transport for this case and thus, ULL population does not increase.

4.3.2 Laser Operating Just-Above Threshold

At 51 kV/cm bias electric field, the laser gain is barely sufficient to support the cavity losses. The band structure in Fig. 4.11(a) shows that the injector ground, i.e., level 9 is not sufficiently aligned with the active region upper lasing level, i.e., level 10 to produce large carrier inversion between the upper and lower lasing levels, i.e., level 10 and 6, respectively. The gain spectrum peak value in Fig. 4.11(b) is not very large.

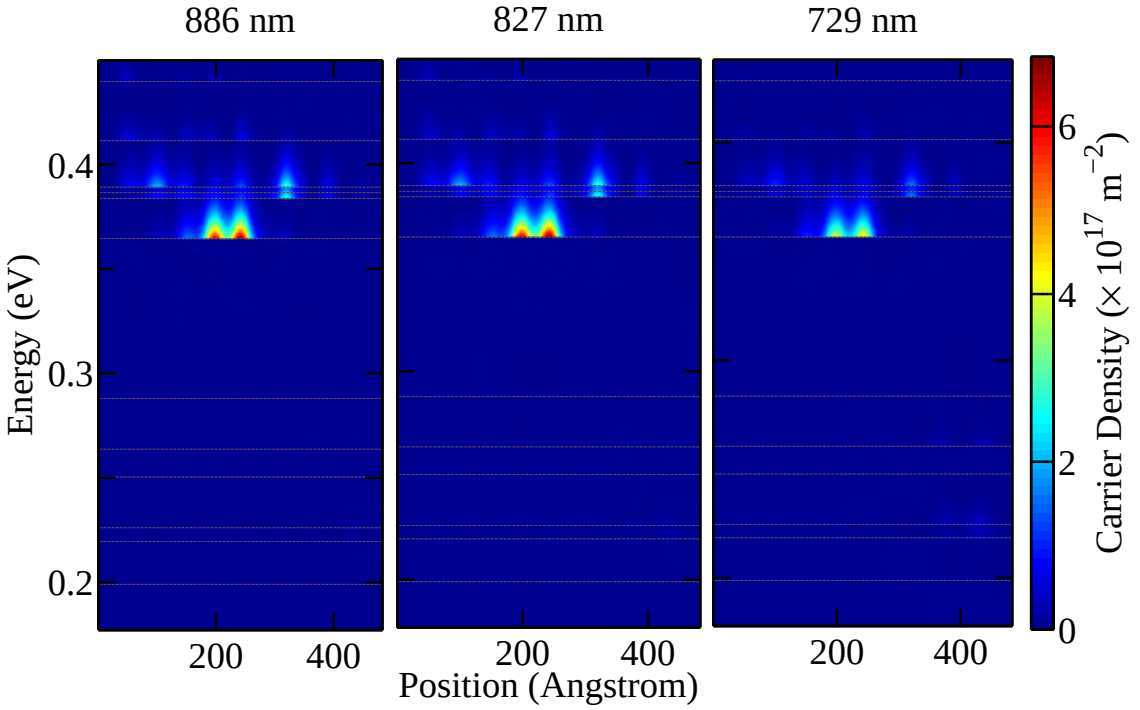

Figure 4.10: Excited carrier distribution over the structure at different subband energies for three different NIR wavelength (a) 886 nm (b) 827 nm (c) 729 nm.

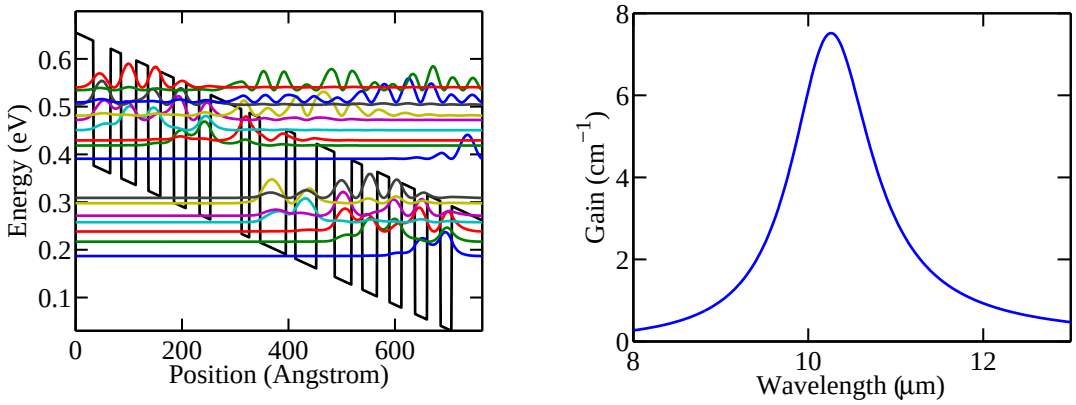

Figure 4.11: (a) Band structure and moduli-squared wavefunctions at 51 kV/cm (b) Gain spectrum at 51 kV/cm. The peak value of the gain spectrum is barely enough to overcome cavity losses.

4.3.2.1 Excitation by 886 nm NIR Pulse

When the QCL is injected with a NIR pulse of wavelength 886 nm, we get similar results as operating bias 41 kV/cm. The gain increases significantly, and the percentage of gain modulation is proportional to the NIR pumping power, i.e., with pumping power increase,

peak gain increases. The output emission wavelength of the QCL also shows a blue shift with the increase of NIR power similar to the operating condition at 41 kV/cm. We report a emission wavelength shift of 0.85 μm for 10 mW NIR pump power. From Fig. 4.12, it is evident that the amount of amplitude modulation is also proportional to the NIR pumping pulse power. The band-structure bending effect due to extra electron hole pairs generated through the optical pumping process is very similar to that of operating at 41 kV/cm.

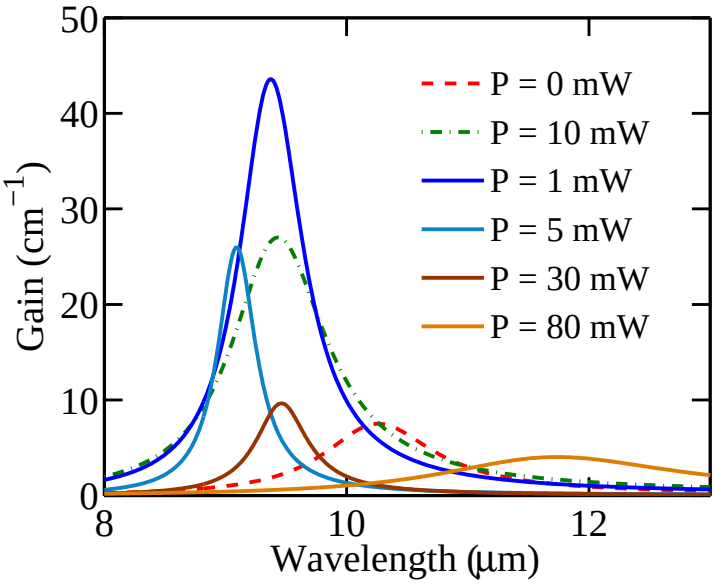

Figure 4.12: Gain spectrum for the structure in [42] after photo-excitation using a NIR pulse of 886 nm for 4 ps. The emission wavelength shows a blue-shift with NIR pulse power increase. The amount of gain increase and emission wavelength blue-shift depend on pumping pulse power.

4.3.2.2 Excitation by 827 nm NIR Pulse

For 827 nm pulse injection, we observe two contradictory phenomena from the gain spectrum plot in Fig. 4.13. For a very high NIR pulse power, the gain spectrum suffers significant decay, whereas, for one-tenth of that previous power, peak gain increases significantly. These two apparently contradictory phenomena can be justified by plotting

the electronic band-structure and carrier distribution in the subbands.

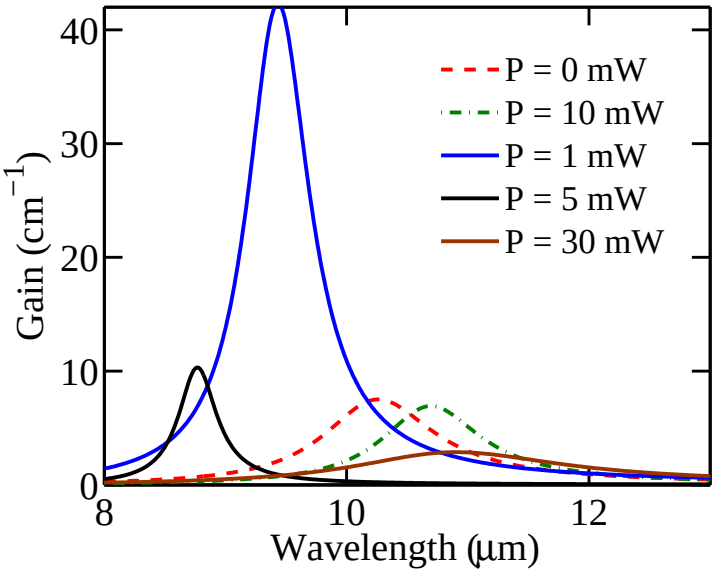

Figure 4.13: Gain spectrum for the structure in [42] at bias electric field 51 kV/cm after photo-excitation using a NIR pulse of 0.827 μm for 4 ps.

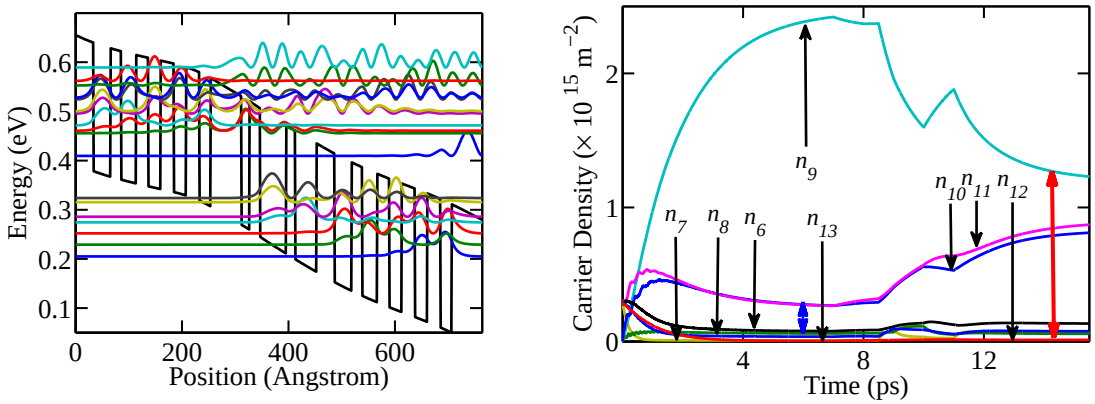

Figure 4.14: (a) Band structure and moduli-squared wavefunctions at 51 kV/cm with excited carrier band bending for NIR pulse output power of 1 mW, coupling 10%(b) Carrier distribution for the condition in (a). Carrier distribution is shown for only the optically important electronic states.

The band bending and carrier distribution for NIR pulse power of 1 mW is presented in Fig. 4.14. As shown from Fig. 4.14(b), the new population inversion after pulse injection is an order of magnitude larger. The upper lasing level (level-9) and the injector ground

(level-10) overlaps, thus ensuring proper transport.

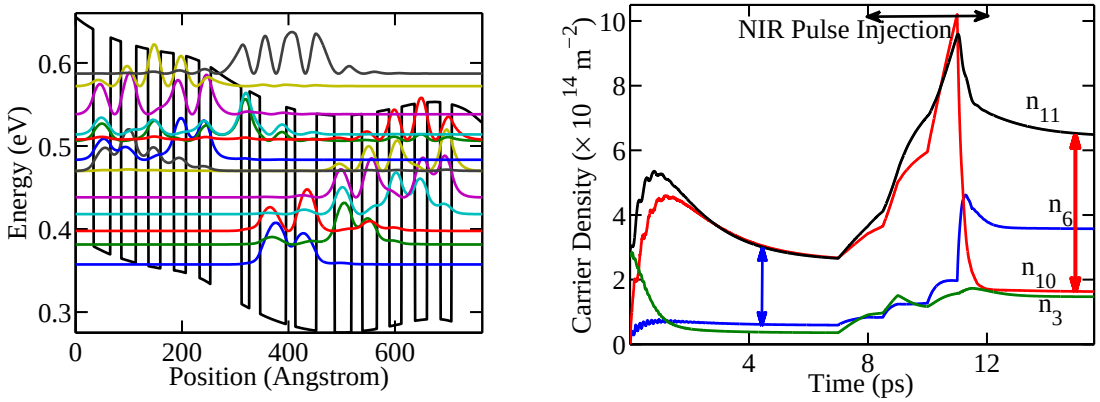

Figure 4.15: (a) Band structure and moduli-squared wavefunctions at 51 kV/cm with excited carrier band bending for NIR pulse output power of 10 mW, coupling 10% (b) Carrier distribution for the condition in (a). Carrier distribution is shown for only the optically important electronic states.

However, for NIR pump power 10 mW, the reverse happens. As it is depicted in Fig. 4.15(a), the new upper lasing level (level-11) and the Injector ground (level -10) are significantly misaligned, which disrupts carrier injection into the upper lasing level. Fig. 4.15(b) validates the misalignment as the new population inversion is almost equal to the original population inversion value, even after extra carrier generation. Thus, peak gain value before and after optical pumping does not change significantly.

4.3.2.3 Excitation by 729 nm NIR Pulse

For 729 nm injected pulse, the excited carrier number is an order of magnitude larger than that of 886 nm as shown in Fig.3.3. These extra carriers creates band-banding which disrupts the lasing operation. Lasing operation ceases even for very small operating power of the NIR pulse (0.1 mW) if the pulse duration is in the ps range.

4.3.3 Laser Operating Well-Above Threshold

We will consider the case when the QCL is biased at 60 kV/cm electric field which is well-above its threshold, and thus is capable of maintaining significant population inversion. We will excite the QCL with NIR pulses of wavelengths 729 nm (1.7 eV), 827 nm (1.5 eV) and 886 nm (1.4 eV).

4.3.3.1 Excitation by 886 nm NIR Pulse

When we inject the laser with a NIR pulse of 886 nm for 4 *ps*, excited carriers change the band structure significantly, thus changing the carrier distribution in the subbands. They also decrease the refractive index of the cavity. In Fig. 4.5 we have plotted the gain spectrum after photo-excitation for 2 different NIR optical power. As it is evident from the Fig. 4.16, gain decreases with increase of NIR optical power which is in agreement with the experimental observations of Refs.[9, 11, 12]. Suchalkin et al. [11, 12] also reported a blue shift in the emission wavelength of the QCL operating well above its threshold after NIR pulse injection, which is also found in our modeling as presented by Fig. 4.16. We have provided the experimental observations from Ref. [11] in Fig. 4.17, where we can verify the blue shift with simultaneous gain decrease of the QCL with NIR optical power.

To find the reason behind gain decrease and blue shift of wavelength, we plot the band-diagram and the time dependent carrier densities in different subbands of the QCL structure at 60 kV/cm with excited carriers when a NIR pulse of 886 nm with optical power 10 mW is injected. From Fig. 4.18(a), we find that the new lasing levels are the 11th and 6th states. In Fig. 4.18(b), we find that, the carrier inversion between the lasing levels (levels: 9 and 7, respectively) before light injection is much greater than the one after carrier excitation (depicted by red double arrow). The reason behind is the band-bending due to excited carriers which disrupts the alignment between the new injector levels (level 9

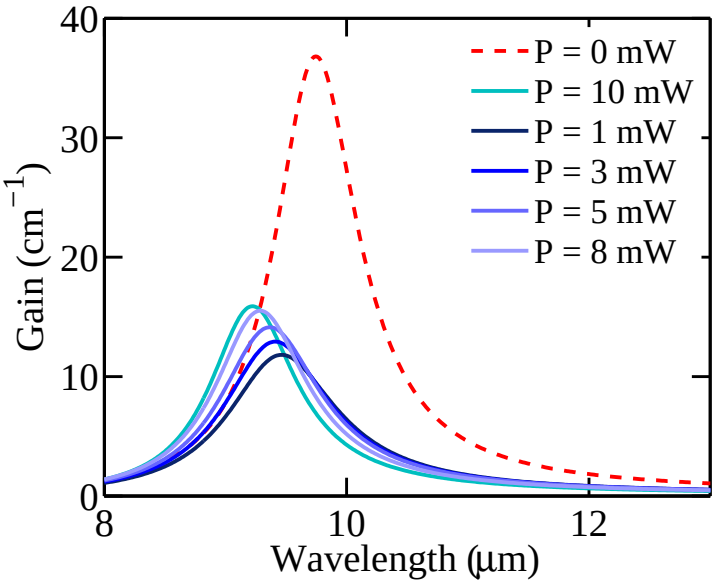

Figure 4.16: Gain spectrum for the structure in [42] at bias electric field 60 kV/cm after photo-excitation using a NIR pulse of 0.886 μm for 4 ps. The emission wavelength shows a blue-shift with NIR pulse power increase.

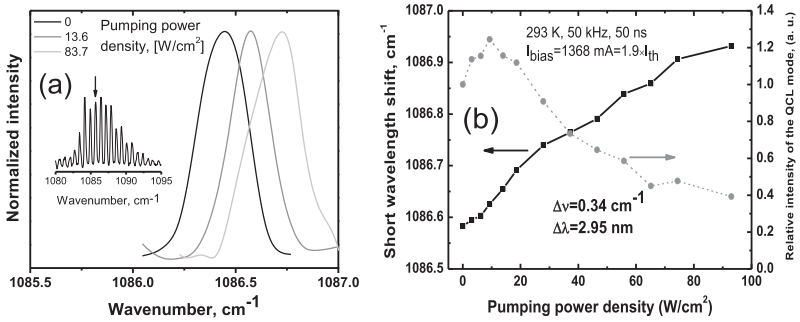

Figure 4.17: Experimental observations from Ref. [11]. (a) Zoom-in of the quantum cascade laser emission spectrum under different optical pumping intensities. A frequency shift of a single longitudinal mode is clearly seen. Inset: emission spectrum of the device. (b) Spectral position of a longitudinal mode in the QCL emission spectrum (left axis) and optical power of the mode (right axis) as a function of optical pump intensity.

and 10) and new upper level (level: 11). As the energy detuning increases between these subbands, less number of carriers can tunnel to upper laser level to create population inversion. Thus, gain decreases. In Table 4.2, we show the change in population inversion and dipole elements for before and after excitation.

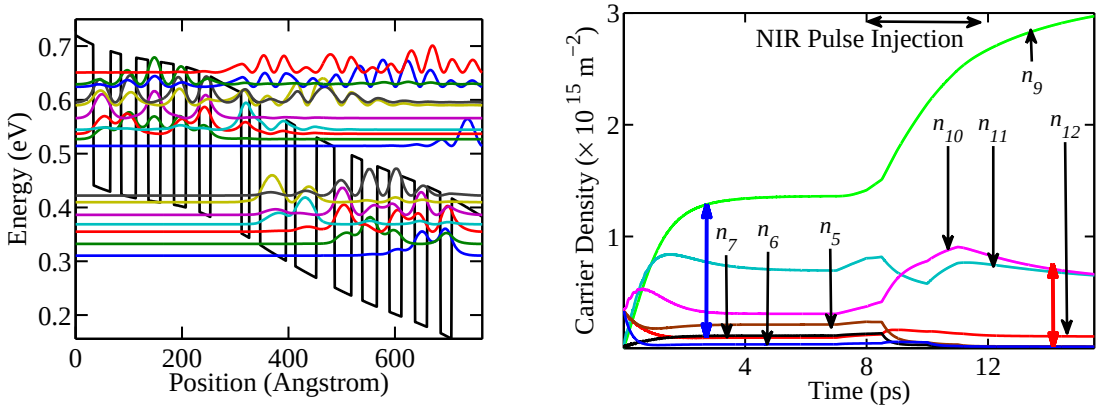

Figure 4.18: (a) Band structure and moduli-squared wavefunctions at 60 kV/cm with excited carrier band bending for NIR pulse output power of 10 mW, coupling 10%(b) Carrier distribution for the condition in (a). Carrier distribution is shown for only the optically important electronic states.

Table 4.2: Determinant parameter comparison for the QCL [42] operating at 60 kV/cm.

	Before Excitation			After Excitation			Trend
	IG = 10	ULL = 9	LLL = 7	IG = 9	ULL = 11	LLL = 6	
$\Delta N_{\text{inversion}}(\times 10^{14})$		12.4			6.36		$\downarrow$
$z_{\text{ULL-LLL}}$ $(\times 10^{-9})$		1.58			1.53		$\downarrow$
$z_{\text{IG-ULL}}$ $(\times 10^{-9})$		5.8			0.69		$\downarrow$
$\Delta E_{\text{IG-ULL}}$ (meV)		8.4			17.6		$\uparrow$

4.3.3.2 Excitation by 827 nm NIR Pulse

We achieve similar results for 827 nm NIR pulse. One very significant observation to make from Fig. 4.19 is to notice the rate of gain reduction. The rate of gain reduction is proportional to NIR pulse power. Also, the amount of blue shift of the emission wavelength of the QCL increases with NIR pulse power increase. Both of these observations have been experimentally observed by the authors in Ref. [9–11].

4.3.3.3 Excitation by 729 nm NIR Pulse

For 729 nm injected pulse, the excited carrier number is an order of magnitude larger than that of 886 nm as shown in Fig.3.3. These extra carriers creates band-banding which

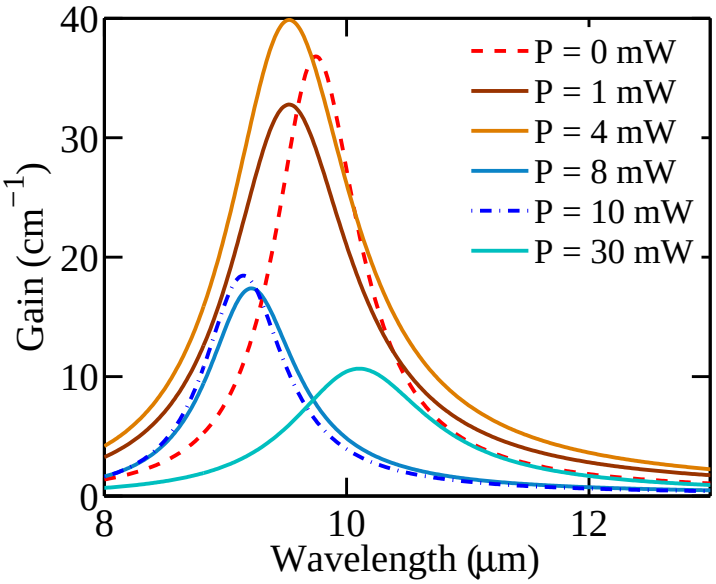

Figure 4.19: Gain spectrum for the structure in [42] at bias electric field 60 kV/cm after photo-excitation using a NIR pulse of 0.827 μm for 4 ps. The emission wavelength shows a blue-shift with NIR pulse power increase.

disrupts the lasing operation. As seen from Fig. 4.20, lasing operation will cease even for very small operating power of the NIR pulse if the pulse duration is in the *ps* range.

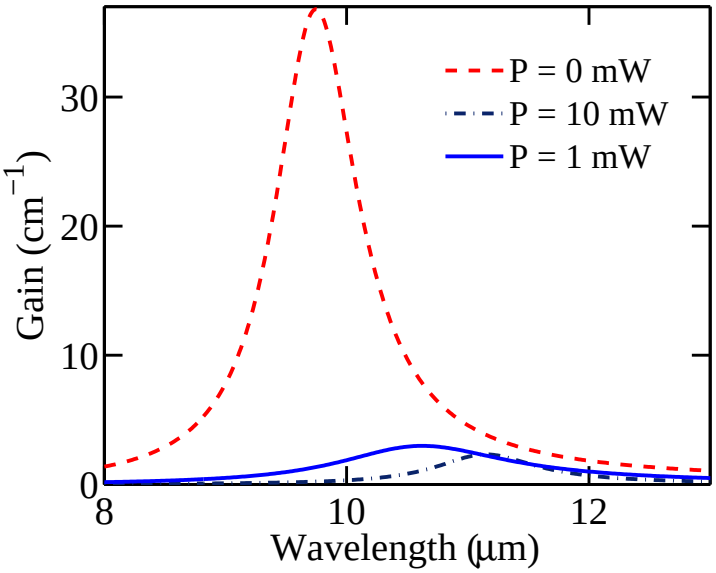

Figure 4.20: Gain spectrum for the structure in [42] at bias electric field 60 kV/cm after photo-excitation using a NIR pulse of 0.729 μm for 4 ps. The lasing action ceases for any of these cases.

4.3.4 Dependence of Gain and Wavelength Modulation on Pumping NIR Wavelength

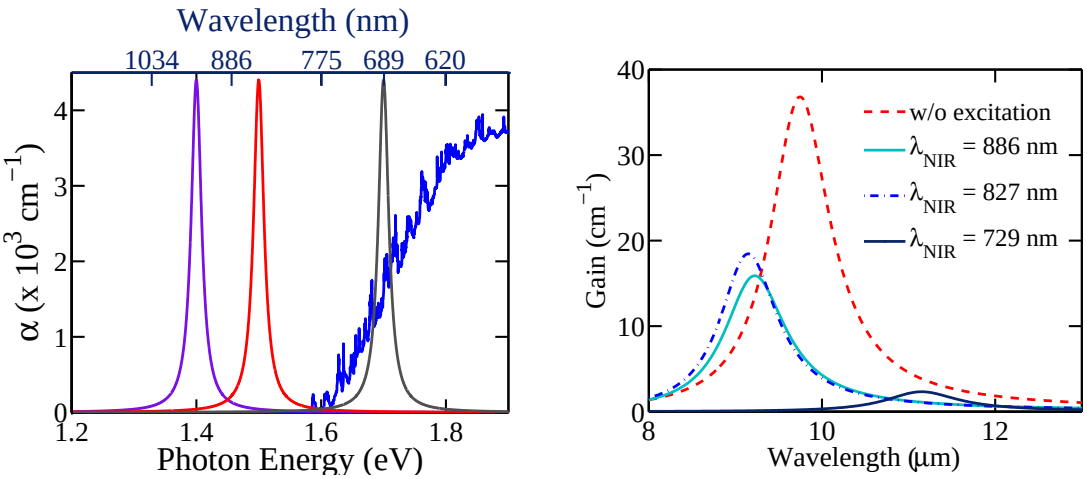

Figure 4.21: (a) Interband absorption spectrum for the QCL structure in Ref. [42] operating at 60 kV/cm. (b) Gain spectrum at bias electric field 60 kV/cm after photo-excitation using NIR pulses of three different wavelengths for 4 ps. The NIR pulse average power is assumed to be 10 mW and coupling of 10%. The gain decreases as the NIR pulse energy increases, and it overlaps more with the interband absorption spectrum.

As discussed in the previous sections, gain of a Mid-IR QCL changes when the device is optically pumped by a NIR pulse. Simultaneously, the emission wavelength of the QCL shows a blue shift with NIR pumping power increase. The change of NIR pumping pulse wavelength have direct influence on the number of electron-hole pairs generated. From the Fig. 4.21, it is apparent that when the NIR pulse energy increases from 1.43 eV, the overlap with the interband apsorption spectrum also increases. Thus number of ehp generated will drastically increase. The spatial carrier distribution will also change depending upon the pumping pulse energy. .

To illustrate the dependence of wavelength, we have plotted the gain spectrum for the discussed QCL structure for three different NIR pump energies, assuming 10 mW NIR pump average power, 10% coupling and 4 ps pulse duration. In all of the cases, the gain decreases; but with the increase of NIR pumping energy and thus, with more overlap with

the interband absorption spectrum, gain is further reduced as shown in Fig. 4.21.

To understand the physics behind the dependence on NIR pumping energy, we refer

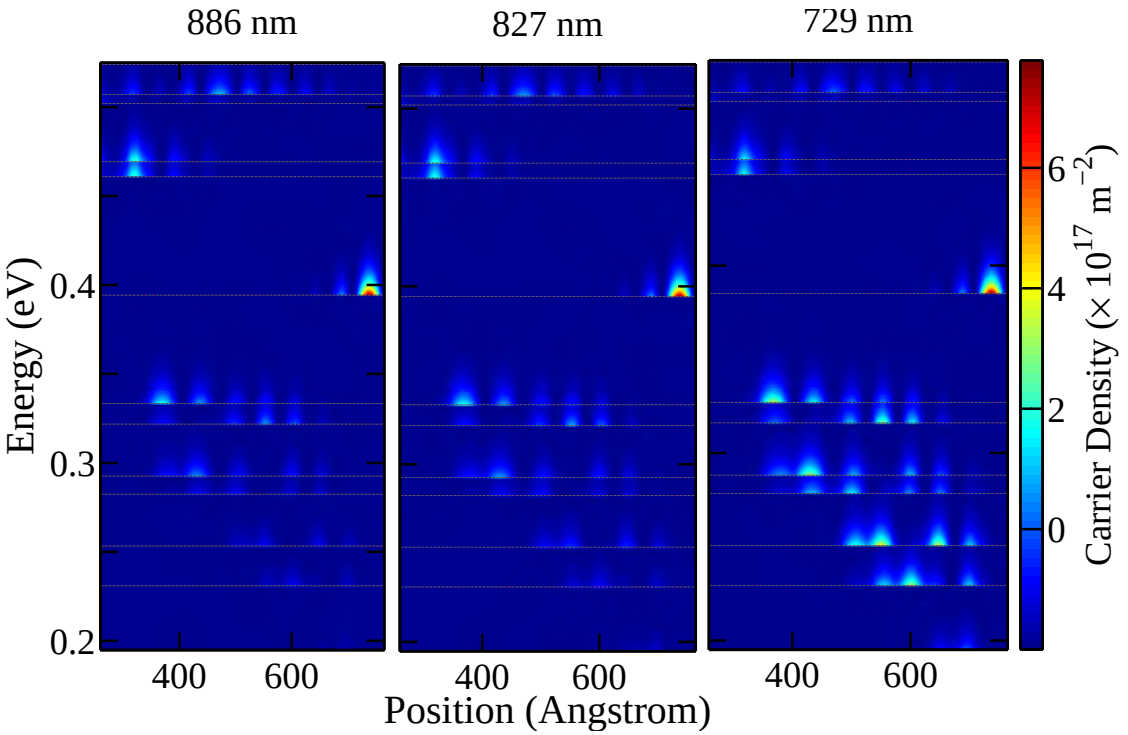

Figure 4.22: Excited carrier distribution over the structure at different subband energies for three different NIR wavelength (a) 886 nm (b) 827 nm (c) 729 nm. The bias is operating at 60 kV/cm

to Fig. 4.22, where we have plotted the spatial distribution of carriers in the different subbands. We see, for 886 nm and 827 nm NIR pulses, more carriers are injected into the lower injector subbands. But, these levels can not contribute to rise ULL population as the band-banding disrupts the proper alignment of the new IG and ULL as shown if Fig. 4.18(b). When 729 nm NIR pulse is injected, more carriers are injected in the upper collector region, which are near to the LLL. Thus, the population of the LLL increases, which will reduce the population inversion. In all three cases, gain decreases, but for the later case the gain-quenching effect is more pronounced.

Now, Fig. 4.23 sums up all our simulation results to give us a proper insight about the change of gain with different wavelengths of NIR pump pulse at different operating con-

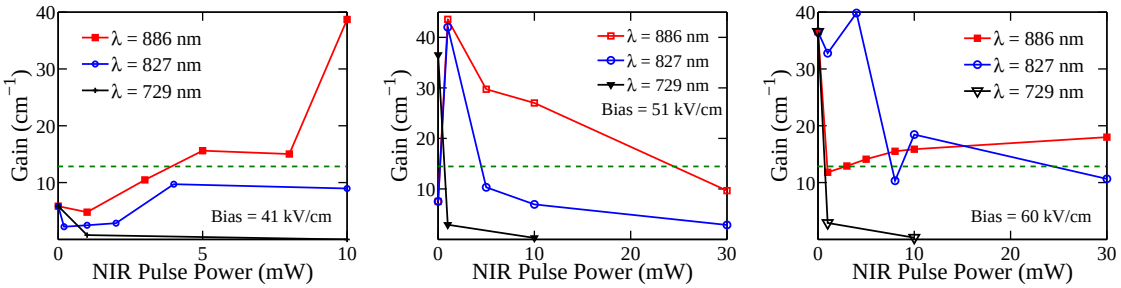

Figure 4.23: Change of gain of MID-IR QCL with injected NIR pulse power and wavelength for different operating bias condition. Here, the green dotted line indicate typical cavity loss value of 15 cm^{-1}. Lasing occurs when gain exceeds the loss coefficient.

ditions. Here, we have plotted the change of gain with respect to the original gain at the operating bias mentioned. We notice that, for 41 kV/cm (below threshold), gain increases with NIR pulse energy for excitation wavelengths of 827 nm and 886 nm (1.4 eV and 1.5 eV, respectively). The laser operates below threshold when the gain crosses the cavity losses, indicated by the green dotted line. For 60 kV/cm operating condition, the gain decreases monotonically with operating NIR pulse energy increase. However, for operating condition just above the threshold (51 kV/cm), the change of gain is complex. Gain increases with NIR pulse of 886 nm, which is resonant with GaAs energy gap, but, gain decreases for non-resonant pumping pulse.

4.3.5 Femto-second Pulse Injection

The quenching effect in mid-IR QCL lasers can also be observed by a femto-second NIR pulse injected into the QCL. Guo et al [43] reported the use of fs-NIR pulses with repetition rate around 250 kHz ($\sim 4\ \mu$s) to experimentally observe quenching effects in mid-IR QCL gain, operating well-above threshold. Using our model for the GaAs/AlGaAs QCL [42], we can also theoretically demonstrate quenching effects in gain of the QCL using NIR power 10-50 mW. In Fig. 4.24, we observe that, about 100% modulation depth can be obtained by using excitation wavelength of 729 nm and 827 nm (1.7 eV and 1.5 eV respectively). Gain can also be positively modulated using pump pulse of wavelength 886 nm (1.4 eV).

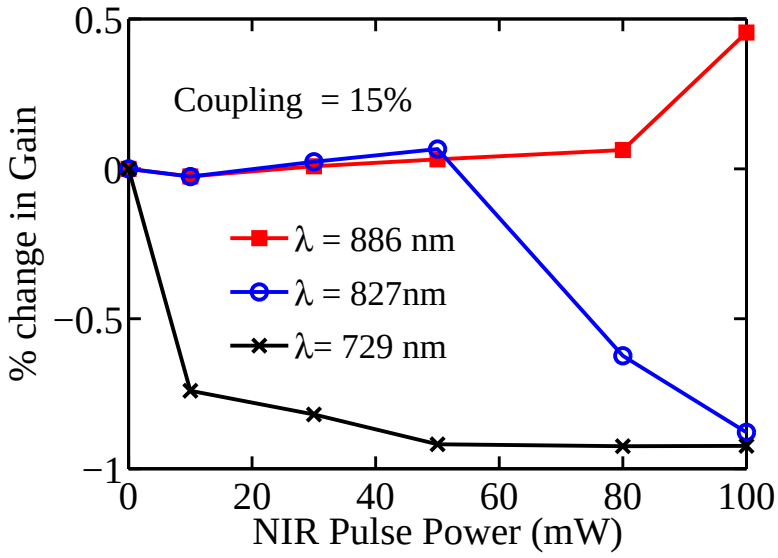

Figure 4.24: Percentage change in gain of a mid-IR QCL by optically pumping with NIR fs-pulses of wavelength 886 nm, 827 nm and 729 nm.

4.3.5.1 Positive gain modulation using 886 nm Pulse

We plot the electronic band structure and carrier distribution in different subbands when the QCL is operated at 60 kV/cm and excited witha NIR pump pulse of wavelength 886 nm and output power of 50 mW in Fig. 4.25. We find that, the band bending due to excited carrier is insignificant, and the population inversion increases due to he excited ehp generated through optically pumping the laser. Thus, gain is positively modulated here.

4.3.5.2 Negative gain modulation using 729 nm Pulse

In Fig. 4.26, we have plotted the electronic band structure and carrier distribution in different subbands when the QCL is operated at 60 kV/cm and excited witha NIR pump pulse of wavelength 729 nm and output power of 50 mW. Contradictory to the case discussed just above, when the NIR pulse of wavelength 886 was used to excite the mid-IR

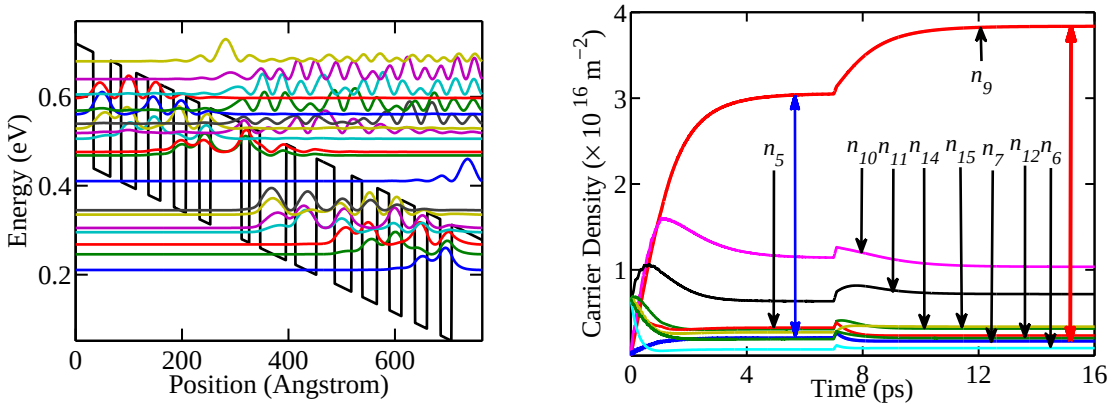

Figure 4.25: (a) Band structure and moduli-squared wavefunctions at 60 kV/cm with excited carrier band bending for 886 nm NIR pulse output power of 50 mW, coupling 15%(b) Carrier distribution for the condition in (a). Carrier distribution is shown for only the optically important electronic states.

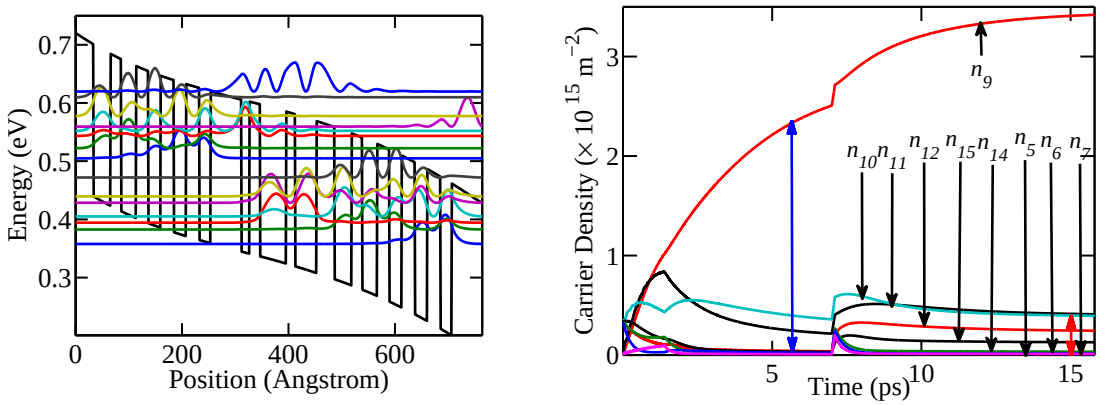

Figure 4.26: (a) Band structure and moduli-squared wavefunctions at 60 kV/cm with excited carrier band bending for 729 nm NIR pulse output power of 50 mW, coupling 15%(b) Carrier distribution for the condition in (a). Carrier distribution is shown for only the optically important electronic states.

QCL, here the band bending due to the extra carrier is significant enough to disrupt the electron transport. The new upper lasing level is level-11 and there is significant reduction in both population inversion and physical overlap between the new ULL and LLL, thus, gain is significantly reduced. Our observation is coherent with the experimental observation of Ref. [43], where they observed quenching of gain of mid-IR QCL is proportional to the NIR pulse power.

4.4 InGaAs/InAlAs QCL Structure

InGaAs/InAlAs material system is a matured technology and used in mid-IR QCl structures prevalently. The InGaAs/InAlAs Fabry-Perot (FP) QCL used in our modeling is based on double phonon depopulation scheme [44] and emits near 9 μm at room temperature at a operating bias of 41 kV/cm. In Fig. 4.27(a), we have plotted the electronic band-structure of the QCL structure where the upper and lower lasing levels are level-12 and level-9 respectively. Carrier density in the subbands are shown in Fig. 4.27(b), where the blue double arrow shows the population inversion between upper and lower lasing levels.

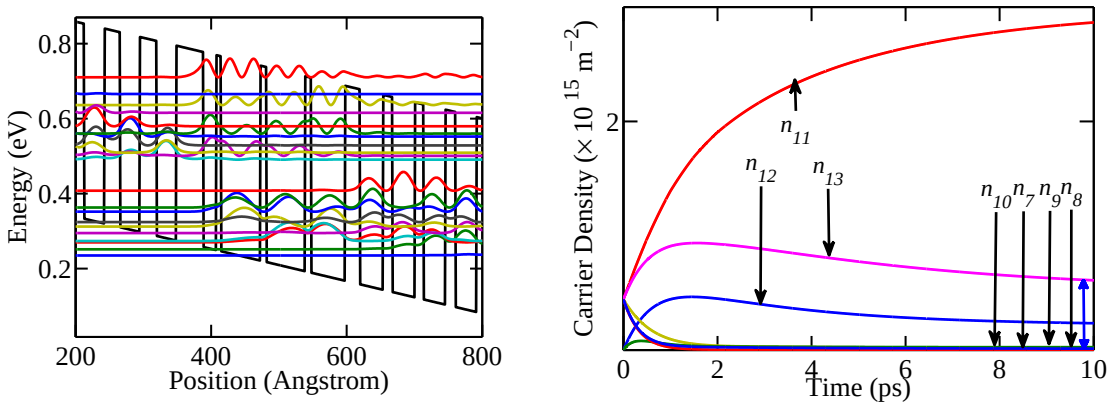

Figure 4.27: (a) Band structure and moduli-squared wavefunctions at 43 kV/cm for the two phonon resonance QCL structure (b) Carrier distribution for the structure. Carrier distribution is shown for only the optically important electronic states. The blue double arrow represents the population inversion.

We apply our model when the mid-IR two-phonon-resonance structure is pumped by a Nd : YVO_3 Q-switch NIR laser emitting at 820 nm (1.51 eV), which is energetically almost twice of bandwidth. From our previous discussions, we expect the gain to reduce. In Fig. 4.28, we observe the gain and wavelength modulation of the mid-IR QCL output through optical pumping using 820 nm NIR source with pulse-width of 4 ps. The gain-quenching is proportional to the NIR pulse power and for NIR power of 10 mW, we can observe more than 50 % modulation depth. Our simulation results are in coherence with

the experimental observations in Ref. [6], where they observed gain-quenching effects and modulation depth to be proportional to NIR pumping power. The wavelength can be tuned over a range of 1.4 μm, theoretically, assuming cavity losses are around 10 cm^{-1}. Emission wavelength shift towards higher photon energy with NIR pulse power increase as observed by Suchalkin et al [11].

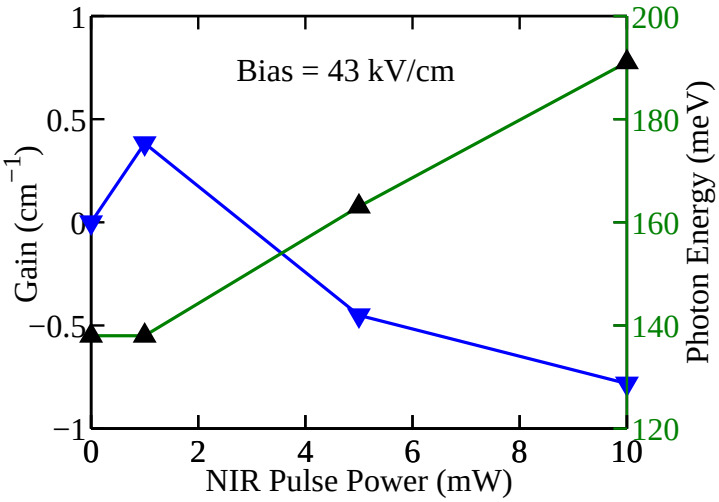

Figure 4.28: Modulation of gain and wavelength for the QCL structure in Ref. [44]. The gain quenching effect is observed and the modulation depth is proportional to NIR power.

To explain the modulation of gain and wavelength, we have plotted the electronic band structure with band bending due to photoexcited carriers in Fig. 4.29(a). We find that, the lasing levels for this condition are level 12 and level 10, respectively. Carriers are injected into all subbands, but the injection rate is higher for high-energy levels (levels 19,20,22) as the NIR pulse energy is almost double of the bandgap. These hot electrons relaxes in level 11 (Injector ground) as shown by the particularly higher carrier density at that level in Fig. 4.29(b). However, due to decreased overlap and coherence between the ULL and IG, the excited carriers can not contribute to population inversion. Thus, population inversion remains almost same even after photoexcitation by the NIR pulse. Because of decreases dipole moment between the new lasing levels, the gain decreases. When the NIR pump power will be increased after this point, less and less overlap between ULL

and LLL will reduce the gain, and thus finally, finally ceasing the lasing action.

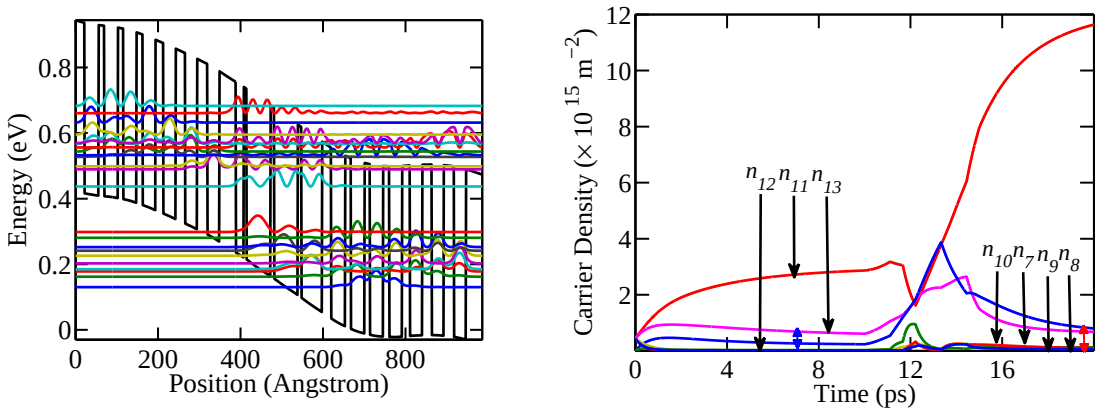

Figure 4.29: (a) Band structure and moduli-squared wavefunctions at 43 kV/cm after NIR injection of 820 nm, with pulse power of 10 mW. (b) Carrier distribution for this condition. Carrier distribution is shown for only the optically important electronic states. The blue and red double arrows represent population inversion.

4.4.1 Femto-second Pulse injection

The number of total electron-hole pairs generated is directly dependent on the pulse duration of the NIR pumping source, as it is evident from Eq. (3.25). For very ultra-short pulses in the range of ~fs, the photoexcited electrons density is one order of magnitude smaller than the QCL's own doping density. Thus, the band-bending effect is not very pronounced. However, the excited carrier relaxation process changes the carrier distribution over the subbands, which eventually effects the gain. In this section, we present the change of gain of mid-IR InGaAs/InAlAs QCL due to NIR pulse injection with pulse duration of femto-seconds. In Fig. 4.30, we have plotted the change of gain and wavelength of QCL due to 1.55 μm NIR injection. We observe that, the gain increases with NIR power as the energy of the NIR is comparable to that of the bandgap of the QCL. We also observe a monotonic shift of QCL emission wavelength to higher photon energy.

For the QCL structure with two phonon resonance active region discussed in Ref. [44],

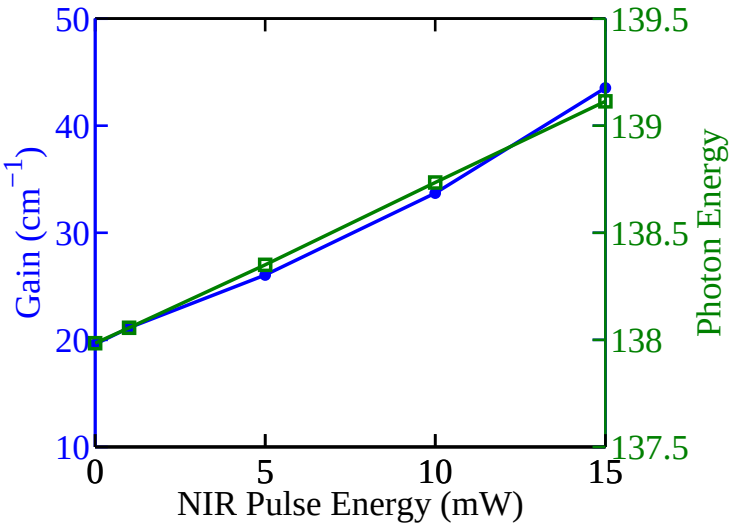

Figure 4.30: Modulation of gain and wavelength for the QCL structure in Ref. [44] when the QCL is pumped by a NIR pulse of 1.55 μm with temporal pulsewidth of 100 fs.

we inject a near-resonant NIR pulse of $\lambda = 1.55\mu$m (0.80 eV) into the cavity of the mid-IR laser. The QCL, operating over its threshold current density, emits at 9 μm. For $\lambda = 1.55$ μm NIR excitation source with a temporal pulse duration of 100 fs, the upper laser level gains more photoexcited carriers than lower laser level ($\Delta N^{\mathrm{ULL}}_{\mathrm{photoexcited}} = 10.2 \times 10^{11}$ m^{-2} and $\Delta N^{\mathrm{LLL}}_{\mathrm{photoexcited}} = 6.7 \times 10^{11}$ m^{-2}), thus, it is anticipated that gain will increase. The maximum value of the extra band-bending potential is around ~ 0.35 meV, which is not significant enough to change the band structure drastically.

In Fig. 4.31(a), we have plotted the carrier distribution with time when the NIR pump pulse power is 3 mW and coupling is 10 %. The injector ground (11th state) gains significant number of carriers; which thermalize though fast intraband relaxation and thus, increase the carrier densities of the levels which are LO phonon energy resonant with it. Thus, level 13 gains electrons though intraband relaxation and so thus the upper lasing level (level 12), which will increase the gain.

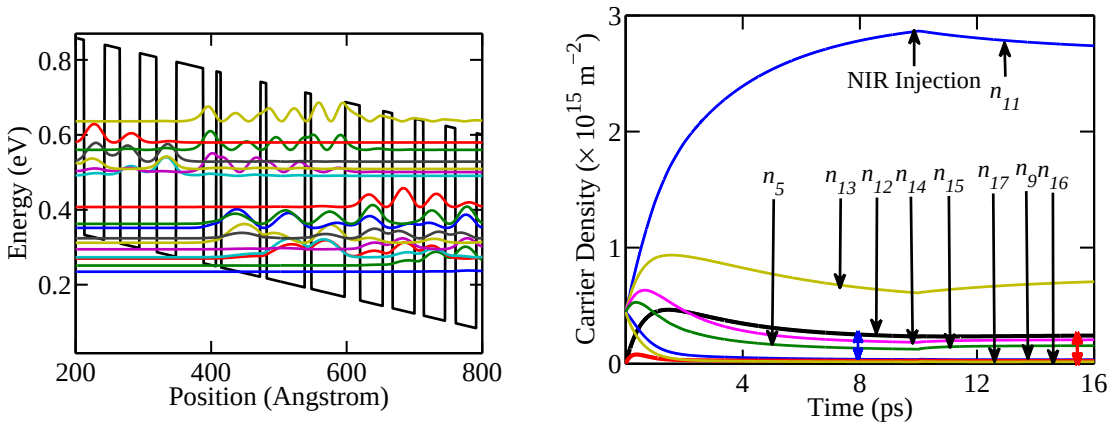

Figure 4.31: (a) Band structure and moduli-squared wavefunctions at 43 kV/cm after NIR injection of 820 nm, with pulse power of 10 mW. (b) Carrier distribution for this condition. Carrier distribution is shown for only the optically important electronic states. The blue and red double arrows represent population inversion.

4.5 Gain from Macroscopic Viewpoint

Until now, all our discussions are focussed on a microscopic point of view. Our simulation time window was 20 ps as the QCL has ultra-fast gain recovery time ($\sim$ 2 ps). We have discussed for both femto-second and pico-second NIR pulse injection and achieved similar results. In our model, we have shown modulation effect on both gain and emission wavelength of mid-IR QCL using NIR pulses for a time window of 20 ps. But to understand what happens after some micro-seconds, we will have to focus on interband transition lifetimes. For a typical interband spontaneous recombination lifetime in the range of μs, the excited electron-hole pairs will recombine and extra carrier effects discussed here (band-bending and associated gain and wavelength modulation) will be reduced. Experimental observations in Ref. [43] agrees with this hypothesis, where they observed gain quenching only for some pico-seconds. Thus, extra carrier effects including gain-quenching were 'momentary' when we look at them from a micro-second time scale.

Zervos et al. [8] varied the Al content in the alloys of QCL structure, and observed that switching only appeared in the 25% samples. Thus, they suggested that the photo-excited

charge is being stored in so-called 'DX centers', metastable electron traps known to be associated with donors in AlGaAs alloys with > 22% Al. Thus, excitonic effects and trapping may effect the interband gain-recovery time for the QCL after NIR pulse excitation, the phenomena in play is open for discussion from a macroscopic point of view.

4.6 Summary

In this chapter, we presented the simulation results showing the effects of NIR light injection into the QCL cavity. NIR light creates electron-hole pairs which increase the conduction subband carrier density.

We notice that, for NIR energy close to the band-gap of QCL, the generated photoexcited electrons contribute to the population injector ground and upper laser level. In this case, the gain monotonically increases with NIR power for femto-second pulses, when the excited carrier induced band-bending is not significant. In contrast, for pico-second NIR pulses, the band-bending changes the electronic structure significantly, and thus, the change is gain depends upon the initial QCL biasing condition and NIR pump power. We have found an increase of gain when the GaAs/AlGaAs QCl structure [42] is biased below threshold, which was experimentally observed in Ref. [8]. However, we found a proportional decrease in gain with NIR power when the QCL is biased well-above its threshold as experimentally observed in Ref. [6, 10–12]. We also observe a blue shift of the emission spectrum which is also proportional to the NIR power.

When the NIR energy is well above the band-gap of QCL, hot electrons come into play and the generated electrons contribute to the population of collector region subbands. This increases the population of the lower lasing level by back-scattering and thus gain is reduced. We also observe a significant shift of emission wavelength with increase of NIR power.

Chapter 5

Conclusion

QCLs are very promising as mid-IR sources for free-space optical communications due to their lower Mie and Rayleigh scattering losses, better scintillation performance, higher modulation bandwidth, and better eye-safe compatibility compared to NIR sources [10]. As NIR optical communications are mature technologies, the ability to convert NIR signal to mid-IR signals will be highly desirable for many future applications. This all-optical modulation scheme will eliminate the parasitic capacitance effects arising from electrical circuitry. Also, wavelength tunability of QCLs by varying the injected NIR power will facilitate its usage as very effective gas sensors for a broader spectrum. Fast wavelength modulation by changing NIR power can be used to circumvent the inherent complexity associated with temperature tuning.

Experimental results in Refs. [6, 8–12, 15, 16, 43] emphasise on the possibility of amplitude and frequency modulation by changing the NIR pump power. However, there is apparent contradiction about positive or negative modulation of mid-IR QCL intensity among the experimental observations. Also, they fail to correlate the the gain change and wavelength shifting with NIR pumping wavelength. Therefore, a detailed theoretical analysis of carrier dynamics in QCL hetersostructure is essential to understand the underlying physics. It will also enable us a precise control over amplitude and frequency

modulation if this technology is to be used effectively.

In this thesis, we have modeled the effects of NIR light injection into the QCL cavity. NIR light creates electron-hole pairs which increase the conduction subband carrier density. The energetic and spatial distribution of the excited carrier depends on NIR wavelength and will determine the change of mid-IR QCL gain and emission wavelength. These extra carriers creates band-bending, which changes the electronic states, and hence, the carrier transport significantly. They also decrease the effective refractive index of the cavity and thus, shift the photon modes to higher values. We include the effect of photo generated excited carrier in the transport model. We solve the transport rate equations to calculate the time-dependent carrier densities at different subbands. We also calculate the band bending potential due to photoexcited electrons and when it is significant, lasing levels and injector levels are changed often. This affects the population distribution and thus, changes the steady state gain. This also changes the emission wavelength significantly as the wavelength is determined by the energy difference between upper and lower lasing levels.

When the NIR energy is close to the band-gap of QCL, the generated photoexcited electrons contribute to the population injector ground and upper laser level. In this case, the gain monotonically increases with NIR power for femto-second pulses, when the excited carrier induced band-bending is not significant. In contrast, for pico-second NIR pulses, the band-bending changes the electronic structure significantly, and thus, the change in gain depends on the initial QCL biasing condition and NIR pump power. We have found an increase of gain when the GaAs/AlGaAs QCl structure [42] is biased below threshold, which was experimentally observed in Ref. [8]. However, we found a proportional decrease in gain with NIR power when the QCL is biased well-above its threshold as experimentally observed in Ref. [6, 10–12]. We also observe a blue shift of the emission spectrum which is also proportional to the NIR power.

When the NIR energy is well above the band-gap of QCL, hot electrons come into play and the generated electrons contribute to the population of the collector region subbands. This increases the population of the lower lasing level by back-scattering and thus gain is reduced. These electrons eventually thermalize to the ground states through intraband processes, but they can not contribute to the population of the next active region upper laser level because of the induced band bending. We also observe a significant shift of emission wavelength with increase of NIR power.

All-optical modulation of QCLs has the possibility to be used in free-space optical communication instead of NIR sources and also in sensor technologies. Thus, a precise control over the modulation depth by changing the NIR wavelength, power or even the QCL material system is essential. Our model, justified by the experimental observations, can play a role in development of this all-optical modulation of QCL.

Bibliography

[1] A. Yariv, *Quantum Electronics*. New York: Wiley, 1989.

[2] J. Wilson and J. Hawkes, *Optoelectronics - An Introduction*. Prentice Hall, 2001.

[3] J. Faist, F. capasso, D. L. Sivco, C. Sirtori, A. L. Hutchinson, and A. Cho, "Quantum cascade laser," *Science*, vol. 264, p. 553, 1994.

[4] R. F. Kazarinov and R. A. Suris, "Possibility of amplification of electromagnetic waves in a semiconductor with a superlattice," *Sov. Phys. Semicond.*, vol. 5, pp. 707–709, 1971.

[5] C. Sirtori and R. Teissier, *Intersubband Transitions in Quantum Structures*, R. Paiella, Ed. New York: McGraw-Hill, 2006.

[6] G. Chen, C. G. Bethea, R. Martini, P. D. Grant, R. Dudek, and H. C. Liu, "High-speed all-optical modulation of a standard quantum cascade laser by front facet illumination," *Appl. Phys. Lett*, vol. 95, p. 101104, 2009.

[7] C. Gmachl, F. Capasso, D. L. Sivco, and A. Y. Cho, "Recent progress in quantum cascade lasers and applications," *Rep. Prog. Phys.*, vol. 64, p. 1533, 2001.

[8] C. Zervos, M. D. Frogley, C. C. Phillips, D. O. Kundys, L. R. Wilson, M. Hopkinson, and M. S. Skolnick, "All-optical switching in quantum cascade lasers," *Appl. Phys. Lett*, vol. 90, p. 053505, 2007.

[9] N. Sekine and I. Hosako, "Intensity modulation of terahertz quantum cascade lasers under external light injection," *Appl. Phys. Lett*, vol. 95, p. 201106, 2009.

[10] G. Chen, C. G. Bethea, and R. Martini, "Quantum cascade laser gain enhancement by front facet illumination," *Opt. Express*, vol. 7, no. 26, pp. 24 282–24 287, 2009.

[11] S. Suchalkin, S. Jung, R. Tober, M. A. Belkin, and G. Belenky, "Optically tunable long wavelength infrared quantum cascade laser operated at room temperature," *Appl. Phys. Lett*, vol. 102, p. 011125, 2013.

[12] S. Suchalkin, G. Belenky, T. Hosoda, S. Jung, and M. A. Belkin, "Distributed feedback quantum cascade laser with optically tunable emission frequency," *Appl. Phys. Lett*, vol. 103, p. 041120, 2013.

[13] T. Beyer, M. Braun, and A. Lambrecht, "Fast gas spectroscopy using pulsed quantum cascade lasers," *J. Appl. Phys*, vol. 93, p. 3158, 2003.

[14] J. Teissier, S. Laurent, C. Manquest, C. Sirtori, A. Bousseksou, J. R. Coudevylle, R. Colombelli, G. Beaudoin, and I. Sagnes, "Electrical modulation of the complex refractive index in mid-infrared quantum cascade lasers," *Opt. Express*, vol. 20, no. 2, p. 11721183, 2012.

[15] T. Yang, G. Chen, C. Tian, and R. Martini, "Optical modulation of quantum cascade laser with optimized excitation wavelength," *Opt. Lett.*, vol. 38, no. 8, pp. 1200–1202, 2013.

[16] T. Yang, C. Tian, G. Chen, and R. Martini, "Non-resonant optical modulation of quantum cascade laser and its application potential in infrared spectroscopy," in *Proc. of SPIE*, vol. 9002, 2014.

[17] S. Datta, *Quantum Phenomena*. Canada: Addison Wesley Publishing Company, 1989.

[18] J. Piprek, *Semiconductor Optoelectronic Devices:Introduction to Physics and Simulation*. London: Academic Press, 2003.

[19] C. Galeriu, "*k.p* theory of semiconductor nanostructures," Ph.D. dissertation, Worchester Polytechnique Institute, 2005.

[20] P. Harrison, *Quantum Wells, Wires and Dots*. West Sussex: Johns Wiley & Sons, 2005.

[21] H. Choi, T. B. Norris, T. Gresch, M. Giovannini, J. Faist, L. Diehl, and F. Capasso, "Femtosecond dynamics of resonant tunneling and superlattice relaxation in quantum cascade lasers," *Appl. Phys. Lett.*, vol. 92, p. 122114, 2008.

[22] C. Sirtori, F. Capasso, J. Faist, A. Hutchinson, D. Sivco, and A. Cho, "Resonant tunneling in quantum cascade laser," *IEEE J. Quantum Electron.*, vol. 34, pp. 1722–1729, 1998.

[23] M. A. Talukder, "Modeling of gain recovery of quantum cascade lasers," *J. Appl. Phys.*, vol. 109, p. 033104, 2011.

[24] J. Faist, F. Capasso, C. Sirtori, and D. L. Sivco, *Intersubband Transitions in Quantum Wells: Physics and Device Applications II*. San Diego: Academic Press, 2000.

[25] R. Ferreira and G. Bastard, "Evaluation of some scattering times for electrons in unbiased and biased single- and multiple-quantum-well structures," *Phys. Rev. B*, vol. 40, no. 2, pp. 1074–1086, 1989.

[26] D. Indjin, P. Harrison, R. W. Kelsall, and Z. Ikonić, "Self-consistent scattering theory of transport and output characteristics of quantum cascade lasers," *J. Appl. Phys.*, vol. 91, pp. 9019–9026, 2002.

[27] P. Harrison, "The nature of the electron distribution functions in quantum cascade lasers," *Appl. Phys. Lett.*, vol. 75, pp. 2800–2802, 1999.

[28] J. Faist, *Quantum Cascade Lasers*. Zurich: Oxford University Press, 2013.

[29] M. A. Talukder, "Analysis of self-induced transparency modelocking of quantum cascade lasers," Ph.D. dissertation, University of Maryland Baltimore County, 2010.

[30] R. C. Iotti and F. Rossi, "Nature of charge transport in quantum-cascade lasers," *Phys. Rev. Lett.*, vol. 87, p. 146603, 2001.

[31] K. Donovan, P. Harrison, and R. W. Kelsall, "Self-consistent solutions to the intersubband rate equations in quantum cascade lasers: Analysis of a $GaAs/Al_xGa_{1-x}As$ device," *J. Appl. Phys.*, vol. 89, pp. 3084–3090, 2001.

[32] T. Kubis, C. Yeh, and P. Vogl, "Quantum theory of transport and optical gain in quantum cascade lasers," *Phys. Stat. Sol. (C)*, vol. 5, pp. 232–235, 2008.

[33] T. Unuma, T. Takahashi, T. Noda, M. Yoshita, H. Sakaki, M. Baba, and H. Akiyama, "Effects of interface roughness and phonon scattering on intersubband absorption linewidth in a gaas quantum well," *Appl. Phys. Lett.*, vol. 78, pp. 3448–3450, 2001.

[34] T. Unuma, M. Yoshita, T. Noda, H. Sakaki, and H. Akiyama, "Intersubband absorption linewidth in gaas quantum wells due to scattering by interface roughness, phonons, alloy disorder, and impurities," *J. Appl. Phys.*, vol. 93, pp. 1586–1597, 2003.

[35] J. H. Smet, C. G. Fonstad, and Q. Hu, "Intrawell and interwell intersubband transitions in multiple quantum wells for far-infrared sources," *J. Appl. Phys.*, vol. 79, pp. 9305–9320, 1996.

[36] P. J. Price, *Two-dimensinal electron transport in semiconductor layers. I. phonon scattering*. New York: Ann. Phys., 1981.

[37] M. Helm, *Intersubband Transitions in Quantum Wells: Physics and Device Applications I*, H. C. Liu and F. Capasso, Eds. San Diego: Academic Press, 2000, vol. 62.

[38] M. Woerner, K. Reimann, and T. Elsaesser, "Coherent charge transport in semiconductor quantum cascade structures," *J. Phys.: Condens. Matter*, vol. 16, pp. R25–R48, 2004.

[39] A. Wittmaan, Y. Bonetti, J. Faist, E. Gini, and M. Giovannini, "Intersubband linewidths in quantum cascade laser designs," *Appl. Phys. Lett.*, vol. 93, pp. 141 103–1–141 103–3, 2008.

[40] S.-C. Lee, I. Galbraith, and C. R. Pidgeon, "Influence of electron temperature and carrier concentration on electron-lo-phonon intersubband scattering in wide $GaAs/Al_xGa_{1-x}As$ quantum wells," *Phys. Rev. B*, vol. 52, pp. 1874–1881, 1995.

[41] S.-C. Lee and I. Galbraith, "The intrasubband and intersubband relaxation of nonequilibrium electron populations in wide semiconductor quantum wells," *Physica E*, vol. 7, pp. 229–232, 2000.

[42] C. Sirtori, P. Kruck, S. Barbieri, P. Collot, , and J. Nagle, "$GaAs/Al_xGa_{1-x}As$ quantum cascade lasers," *Appl. Phys. Lett*, vol. 73, pp. 3486–3488, 1998.

[43] D. Guo, H. Cai, M. A. Talukder, X. Chen, A. M. Johnson, J. B. Khurgin, and F.-S. Choa, "Near-infrared induced optical quenching effects on mid-infrared quantum cascade lasers," *Appl. Phys. Lett*, vol. 104, p. 251102, 2014.

[44] J. Faist, D. Hofstetter, M. Beck, T. Aellen, M. Rochat, and S. Blaser, "Bound-to-continuum and two-phonon resonance quantum-cascade lasers for high duty cycle, high-temperature operation," *IEEE Journal of Quantum Electronics*, vol. 38, no. 6, pp. 533–546, 2002.